RSC Advances

REVIEW

View Article Online
View Journal | View Issue

Check for updates

Cite this: *RSC Adv.*, 2024, **14**, 18617

Magnetoresistance (MR) properties of magnetic materials

Okvarahireka Vitayaya,[a] Phahul Zhemas Zul Nehan,[a] Dicky Rezky Munazat,[a] Maykel T. E. Manawan[bc] and Budhy Kurniawan *[a]

In this review, the classification of magnetic materials exhibiting magnetoresistive properties is the focus of discussion because each material possesses different magnetic and electrical properties that influence the resulting magnetoresistance (MR) values. These properties depend on the structure and mechanism of the material. In this overview, the classification of magnetic materials with different structures is examined in several material groups, including the following: (1) perovskite structure (ABO_3), (2) alloy, (3) spinel structure, and (4) Kagome magnet. This review summarizes the results of each material's properties based on experimental findings, and serves as a reference for studying the characteristics of each material.

Received 15th March 2024
Accepted 21st May 2024

DOI: 10.1039/d4ra01989j

rsc.li/rsc-advances

Open Access Article. Published on 11 June 2024. Downloaded on 2/18/2026 10:19:39 AM.
This article is licensed under a Creative Commons Attribution-NonCommercial 3.0 Unported Licence.

1. Introduction

Magnetoresistance (MR) is the response of a conductor's resistance to an external magnetic field and is associated with the mechanism of charge carrier scattering.[1] The properties of MR are classified into four types, anisotropic magnetoresistance (AMR), giant magnetoresistance (GMR), tunneling magnetoresistance (TMR), and colossal magnetoresistance (CMR). Research on magnetoresistance began with the discovery of the anisotropic magnetoresistance (AMR) effect by William Thomson (Lord Kelvin) in 1856. In his research, William Thomson conducted tests on several samples, including iron, nickel, and brass, to determine the conductivity of each material under the influence of various magnetic field orientations. Thomson found no change in resistance owing to the influence of the magnetic field in brass. However, in iron and nickel materials, an increase in resistance occurred in parallel magnetic field orientations, whereas in perpendicular magnetic field orientations, the resistance decreased. This forms the basis of the magnetoresistance phenomenon. However, in its early discovery, only a 2% decrease in the resistance occurred under

[a]*Department of Physics, Universitas Indonesia, Depok, 16424, Indonesia. E-mail: budhy.kurniawan@sci.ui.ac.id*
[b]*Research Center for Advanced Materials, BRIN, Serpong 15314, Indonesia*
[c]*Faculty of Defense Technology, Indonesia Defense University, Bogor 16810, Indonesia*

Okvarahireka Vitayaya

Okvarahireka Vitayaya is presently pursuing an MS in materials science at Universitas Indonesia jointly with Dr Budhy Kurniawan R. and Maykel T. E. Manawan through 2023. In 2022, she graduated with a bachelor's degree in physics from Universitas Riau. Through the Indonesian Ministry of Education, Culture, Research and Technology, she was awarded a Pendidikan Magister menuju Doktor untuk Sarjana Unggul (PMDSU) scholarship program for her studies. Her area of interest is the properties of magnetic materials, particularly those based on lanthanum manganite, such as their enormous magnetoresistance.

Phahul Zhemas Zul Nehan

Phahul Zhemas Zul Nehan graduated with a bachelor's degree in Physics from Institut Teknologi Sepuluh on October 2023. He is currently pursuing a master's degree in materials science at Universitas Indonesia's Department of Physics, working with Prof. Dr Darminto, Dr Maykel T. E. Manawan, and Dr Budhy Kurniawan as mentors. He was supported in his studies by the Indonesian Ministry of Education, Culture, Research, and Technology through the Pendidikan Magister menuju Doktor untuk Sarjana Unggul (PMDSU) scholarship program. His areas of interest in materials science are mostly in the characterization of energy storage, magnetic, and composite materials.

© 2024 The Author(s). Published by the Royal Society of Chemistry

Open Access Article. Published on 11 June 2024. Downloaded on 2/18/2026 10:19:39 AM. This article is licensed under a Creative Commons Attribution-NonCommercial 3.0 Unported Licence.

the influence of low magnetic fields at room temperature. However, this study did not show any significant development in the MR phenomenon. It wasn't until the early 1970s that the demand for magnetic data storage systems increased, which drove increased research in the field of magnetic sensors.[2] In the 1970s, research related to TMR began to emerge. Julliere first studied the TMR effect in 1975. He discovered a magnetic tunnel junction (MTJ) in the Fe/Ge–O/Co multilayer, which showed an MR value of 14% at a temperature of 4.2 K. Subsequently, Maekawa and Gafvert also observed TMR. However, research related to TMR has received little attention for more than a decade because there was not studied further at room temperature. MR properties regained attention in 1988 with the discovery of the giant magnetoresistance (GMR) phenomenon in magnetic multilayers.[3] In 1988, GMR was first reported in thin Fe/Cr layers within nanometer structures containing various types of ferromagnetic metals, and practically, GMR was used in hard disk drives (HDD).[4] This research pushed the boundaries of William Thomson's previous, enabling the generation of larger resistance changes. The results from the Fe–Cr–Fe layers showed resistance changes of 10% to 50% at low temperatures. This remarkable finding was acknowledged by the 2007 Nobel Prize in Physics. Despite being a highly significant discovery, there are constraints in the development of GMR. Some of these include the experimental samples they created involving complex production methods, such as the single-crystal growth method to form uniform film layers. However, the production method is not suitable for large-scale production. The best results were obtained at low temperatures (50% at 4 K by Fert and 10% at 5 K by Grunberg).[2] The mechanism of the GMR differs from that of the AMR. Magnetization in ferromagnetic materials arises from the spin-splitting effect, resulting from the quantum exchange interaction between electrons. The spin-split band structure leads to different spin-up and spin-down states at the Fermi level, resulting in changes in conductivity properties. In AMR, the difference in resistance because of the application of magnetic field orientations parallel or perpendicular result from of the difference in the scattering cross-sectional area induced by electron spin–orbit coupling. In contrast, the GMR is based on the spin-dependent scattering effect, which explains the anomalies in solid ferromagnetic materials with impurities. The solution lies in the "two-channel model," which treats spin-up and spin-down electrons as relatively independent conduction channels, where spin-flip scattering between the two channels is neglected. Because of the spin-polarized band structure of ferromagnetic transition metals, the mean free path of electrons is much smaller, as electrons can transition to partially filled d states, leading to stronger scattering and higher resistivity. The unfilled d states are also responsible for ferromagnetism, thus establishing a direct relationship between the electrical transport and magnetic properties.[5] GMR technology opens up opportunities for various applications, such as position sensors,

Dicky Rezky Munazat

Dicky Rezky Munazat graduated from Universitas Indonesia in 2020 with a Master's degree in Materials Science after earning his Bachelor's degree in Physics in 2018. He works as a research assistant and support staff member at Universitas Indonesia's Department of Physics. He is currently working on a doctorate in materials science at Universitas Indonesia's Department of Physics, guided by Dr Budhy Kurniawan and Maykel T. E. Manawan. His areas of interest are the properties of magnetic materials, such as the magnetocaloric effect and massive magnetoresistance, and the synthesis and characterization of ceramic magnetic materials using X-ray/neutron diffraction crystallographic analysis.

Maykel T. E. Manawan

Maykel T. E. Manawan obtained his Bachelor's, Master's, and Doctorate degrees in Physics in 2005, 2009, and 2014. He has been a researcher at the National Research and Innovation Agency since 2022 and a lecturer at Universitas Pertahanan Indonesia since 2018. Other experiences include joining and working for Bruker-AXS Indonesia (since 2017) and the International Center for Diffraction Data (ICDD since 2020). Applications of crystallography, quantum crystallography, batteries, X-ray/neutron diffraction analysis, magnetic materials, and materials science are among his areas of interest.

Budhy Kurniawan

Budhy Kurniawan graduated from Universitas Indonesia with a Bachelor's and Master's degree in Physics (1992 and 1995), and Tokyo Institute of Technology, Japan, awarded him a PhD in the field of condensed matter physics (2000). He is currently an Associate Professor at Universitas Indonesia's Department of Physics. His areas of interest in study are the properties and characterization of quantum spin systems, as well as magnetic materials such as magnetoresistance, magnetocaloric effect, microwave absorber materials, multiferroic materials, and thermoelectric phenomena.

© 2024 The Author(s). Published by the Royal Society of Chemistry

Open Access Article. Published on 11 June 2024. Downloaded on 2/18/2026 10:19:39 AM. This article is licensed under a Creative Commons Attribution-NonCommercial 3.0 Unported Licence.

biomagnetism, magnetic random access memory (MRAM), and current sensors. In 1993, the first automotive sensor emerged, more than four years before using GMR in read-head sensors for hard disks. MR sensors have also been applied in a wider range of fields, from the automotive sectors to biophysics. In recent years, GMR have been developed for current sensors, storage function sensors, and biotechnology applications. Colossal magnetoresistance (CMR) is relatively new compared with other MR effects.[2] CMR is typically associated with spin polarization induced by a magnetic field, resulting in reduced spin scattering and resistance. CMR is related to the double-exchange (DE) mechanism, which has potential commercial applications in magnetic storage media.[6]

It has been reported that MR has been increasingly drawing attention in the past few decades because of its wide-ranging applications.[15–18] One application of the MR effect is in computer memory and storage technology.[19] In sensor systems, the MR effect is also widely utilized, such as in biosensing, biochips, and the emerging field of "spintronics" commonly known as spin electronics or magnetoelectronics. This field focuses on investigating the spin properties of electrons to enhance the efficiency of electronic devices and to discover new properties.[20] Magnetic materials with high MR values and Curie temperatures (T_C) close to room temperature exhibit promising prospects for applications in the manufacturing of uncooled infrared bolometers and magnetic sensor devices.[21] In its development, several material structures that exhibit good MR values have been discovered, including perovskite materials,[7–9,22,25] alloy,[13,17,23] Kagome magnets,[10,13–16,24] and spinel.[11,12,26,27,29] In the past few decades, perovskite materials in manganese oxide compounds with mixed valence states have become one of the most intriguing research topics in the study of magnetic materials. This is because of their highly varied multifunctional properties in terms of magnetism, making them suitable for diverse applications such as magnetic refrigeration, spintronics, and solid oxide fuel cells (SOFC). However, what makes them particularly interesting are the intrinsic phase differences based on various interactions related to the coexistence of regions with significantly different magnetic, electrical, and structural characteristics. The fundamentals of the interplay between the electronic and magnetic phase states have been extensively studied and have garnered much attention. This can explain a wide range of phenomena in all strongly correlated electron systems in the presence of phase coexistence.[28] Based on a comprehensive review of the MR phenomena from the various material groups above, this review will discusses the interconnected properties of each material that influence the resulting MR values. The characteristics of these materials were based on conducted previously experimental data, providing a reference for determining material types with superior properties and demonstrating the best MR values.

2. Magnetoresistance classification

2.1 Giant magnetoresistance (GMR)

Giant magnetoresistance (GMR) is a phenomenon in which the resistance of a material can rapidly change owing variations in the external magnetic field.[29] GMR has excellent potential as a magnetic field sensor, possessing both magnetic and electrical properties. It has been widely developed for various applications such as sensor measurements, current sensing, linear and rotational position sensors, data storage, and magnetic random access memory (MRAM).[30] The GMR system candetect extremely low magnetic fields.[31] GMR is a quantum mechanical effect that was first observed in 1988 in thin-film materials consisting of multiple layers of ferromagnetic Fe separated by non-magnetic Cr.[32] Giant magnetoresistance (GMR) is defined as the ratio $(R_{AP} - R_P)/R_P$, where R_{AP} is the resistance in antiparallel materials and R_P is the resistance of parallel materials. The GMR effect is utilized to change the magnetization orientation in adjacent magnetic metal layers, where the film thickness must be smaller than the average free path of the electrons. Fig. 1A(i) shows that when the magnetic layers are anti-parallel, it results in a higher probability of scattering because spin-up and spin-down electrons scatter more strongly, resulting in higher resistivity. In contrast Fig. 1A(ii) shows that when the magnetic layers are parallel, the current is mostly carried by spin-up, which can easily pass through the material layers experiencing weak scattering, resulting in lower resistance.[33] The electrical transport properties are influenced by three parameters, namely: spin-dependent scattering within the layers, spin scattering at the interfaces between layers, and resistivity dependent on the magnetization orientation in the magnetic layers.[34] Electrons in magnetic materials exhibit different resistances and average free path lengths owing differences in the density of states at the Fermi level ($N(E_F)$) for two different spin states when an external magnetic field is applied.

The GMR effect is generally explained by spin-dependent electron scattering. In the case of ferromagnetic layers with parallel magnetization directions, only one type of electron is strongly scattered, resulting in low resistivity. In the case of antiparallel magnetization directions, both types of electrons were significantly scattered, resulting in high resistivity.[35] GMR is not only found in magnetic multilayers but also in magnetized metallic grains, such as Co or Fe. The grain size nanoscale and the magnetic moments of the grains are nearly isolated from each other.[36] As in the study by John *et al.*, the $Co_{20}Cu_{80}$ sample shows an MR value of 18% with the application of a magnetic field of 50 kOe.[37]

2.2 Colossal magnetoresistance (CMR)

Colossal magnetoresistance (CMR) is the extraordinary increase in electrical conductivity in the presence of a magnetic field. CMR is classified into two types based on origin: intrinsic CMR and extrinsic CMR. In intrinsic CMR, perovskite manganite is formed by the double exchange mechanism and is typically observed at relatively high magnetic field scales and narrow temperature ranges. On the other hand, extrinsic CMR, or what is called low field magnetoresistive (LFMR), is usually found in polycrystalline materials and arises owing to irregular grain boundaries. This extrinsic MR effect is caused by spin-polarized tunneling (SPT) or spin-dependent scattering (SDS) during

Open Access Article. Published on 11 June 2024. Downloaded on 2/18/2026 10:19:39 AM.
This article is licensed under a Creative Commons Attribution-NonCommercial 3.0 Unported Licence.

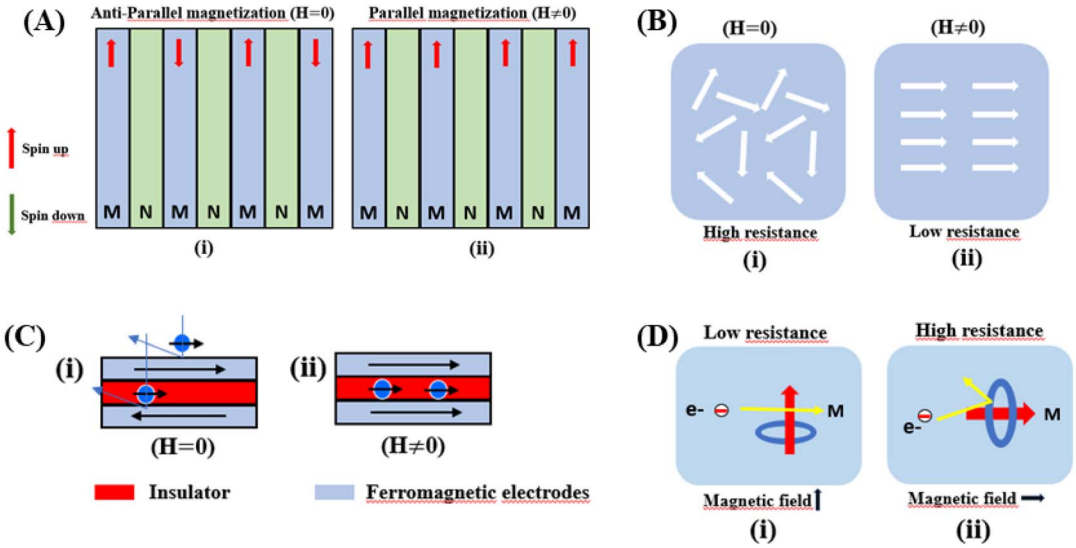

Fig. 1 [A] (i) Antiparallel (low resistance) and (ii) parallel magnetization (high resistance), where N represents the non-magnetic layer and M represents the magnetic layer. [B] (i) Random spin orientation (high resistance), (ii) spin alignment because of the influence of an external magnetic field (low resistance). [C] (i) Magnetic scheme in the TMR effect antiparallel state, (ii) parallel state. [D] Scheme of the AMR effect: (i) *M* parallel to *i* and (ii) *M* perpendicular to *i*.

electron transport across the grain boundaries. LFMR is temperature-independent and occurs at low magnetic fields. LFMR was observed over a wide temperature range below the Curie temperature (T_C). LFMR increased with decreasing grain size. This is because a higher number of grain boundaries will increase spin disturbances, acting as electron scattering centers and resulting in a high resistance without applying a magnetic field. Then, with the application of a small magnetic field, it can initially align irregular spins, reducing electron scattering and resulting in LFMR.[38–41] Fig. 1B(i) is associated with the spin polarization induced by the magnetic field, which inhibits spin scattering and reduces electrical resistance. A characteristic of CMR materials is their ability to rapidly align magnetic spins, thereby reducing electron scattering and electrical resistance in the material. This condition makes the material highly conductive (Fig. 1B(ii)).[42]

The CMR phenomenon cannot be solely explained by the double exchange (DE) mechanism. The CMR is also influenced by several interactions, such as the Jahn–Teller (JT) polaron and phase separation. The CMR effect is categorized into two types, namely intrinsic MR and extrinsic MR. Intrinsic MR which are expressive at high magnetic fields, whereas extrinsic MR is significantly more pronounced at low magnetic fields (<0.2 T).[22] CMR is explained by the concept of double exchange (DE), which considers the transfer of electrons or holes between two Mn atoms through the 2p orbital of oxygen atoms as intermediaries. There is also a polaronic effect related to the dynamic distortion of octahedral MnO_6.[43] Polarons involves collective electron motions in a distorted lattice that serve as key transport features in manganite materials. In the development of CMR, studies related to polarons, such as polaron ordering and the transition from polaron transport to metal transition. Among various interactions, two basic types of electron-lattice coupling are important in manganites. One of these is the influence of the crystal structure on electron transportation and bonding. Different ion radii at the A sites result in different internal pressures on the Mn–O–Mn bonds. This lattice distortion leads to the transition from the ideal cubic structure to hexagonal, rhombohedral, and orthorhombic structures, which can affect the Mn–O–Mn bond angles (<180°) because of the influence of rigid rotations of the MnO_6 octahedra. This results in a reduction in the width of the e_g conduction band, conductivity, and ferromagnetic DE.[44] The distortion at the Mn site is key to explaining the mechanism of the polaron transition.[45] The electronic and lattice properties are highly influenced by the distribution of Mn–O bond lengths. The distorted Mn–O bonds above T_C are consistent with Jahn–Teller distortions in the MnO_6 octahedra.[46] During the electron transfer process, there is a dynamic and cooperative influence of the Jahn–Teller type of distortion. Conduction in manganites is described by electron transfer, for example, from Mn^{3+} ions to the nearest Mn^{4+} ion orbitals through the 2p orbital of oxygen. When the electron spin t_{2g} from Mn combines in a ferromagnetic manner, the conduction band opens when there is a regular exchange of Mn^{3+}/Mn^{4+} sites. The ease of conduction depends on the Mn–O–Mn angle approaching 180°, which improve the conductivity. The Mn–O–Mn angle depended on the size of the A cation. The transition from a paramagnetic insulator to ferromagnetic metal around T_C with the application of a magnetic field is explained by the alignment of electron spins at the t_{2g} level, allowing electron transport at the e_g level.[47] In thin films, the resistivity is twice that of the crystal and six times that of the intrinsic resistivity of the stoichiometric bulk material. This indicates that the resistance of the grain boundary was dominant. The resistivity of the thin films can be expressed as $R_i + R_{gb}$, R_i is the intrinsic resistance, and $R_{gb} = n \times$

© 2024 The Author(s). Published by the Royal Society of Chemistry

Open Access Article. Published on 11 June 2024. Downloaded on 2/18/2026 10:19:39 AM. This article is licensed under a Creative Commons Attribution-NonCommercial 3.0 Unported Licence.

r_{gb}/A, represents the extra resistance because of n grain boundaries in a sample of cross-sectional area A.[48]

2.3 Tunneling magnetoresistance (TMR)

Tunneling magnetoresistance (TMR) has an effect similar to that of GMR, however TMR includes a non-magnetic insulating layer (instead of a conducting layer). The insulating layer typically has 1–2 nm thickness, which allows electrons to tunnel through it. This type of sensor is known as the magnetic tunnel junction (MTJ). The materials used for the insulating layer are typically Al_2O_3, Ga_2O_3, MgO, and graphene. TMR sensors can detect micro to nanosized particles. MTJs exhibit the most sensitive magnetic resistance, with an MR ratio of 20–50%.[31]

In the TMR effect, electrons move from one ferromagnetic (FM) layer to another through the tunneling effect. In this tunneling process, electrons find a free path to the tunnel in the parallel magnetization direction, making the electron transport process easier than antiparallel magnetization when the electron state at the barrier is polarized (Fig. 1C(i) and (ii)). The TMR effect can be defined as $(R_{AP} - R_P)/R_P$, where R_{AP} is the resistance of antiparallel materials and R_P is the resistance of parallel materials. The TMR effect was first observed by Julliere in 1975 when a tunnel junction between two FM films (Fe–Ge–Co tunnel junction) was created. The key point of the TMR phenomenon is the dependence of the tunnel resistance of ferromagnetic junctions on the orientation of magnetic moments. This effect is similar to that of GMR in magnetic multilayers, where the resistance depends on the orientation of magnetic moments separated by nonmagnetic metallic layers. The TMR effect is typically observed in simple planar junctions and also exists in more complex junctions, such as mesoscopic double-barrier junctions, and junctions including granular systems.[49]

Magnetic Tunnel Junctions (MTJs) exhibiting Tunneling Magnetoresistance (TMR) have become the core of modern magnetic storage. Most of MTJs use FeCo alloy magnetic electrodes that are body-centered cubic (BCC)-centered, and directly interfacing with the MgO barrier (FeCo MgO-MTJs). The resulting TMR ratio exceeded 1000% in the polycrystalline FeCo/Mg MTJs at cryogenic temperatures. This thousandfold effect is attributed to the nearly complete spin polarization of tunneling electrons in the energy band of the Bloch electronic states. The TMR value can rival that of MTJs with half-metal electrodes such as Co_2 (Mn, Fe) Si.[50]

2.4 Anisotropic magnetoresistance (AMR)

The anisotropic magnetoresistance (AMR) effect results in electrical conductivity that depends on the magnetization orientation and the current density vector. In ferromagnetic materials, the resistivity is high when the magnetic field is parallel to the current, and the resistivity was low when the magnetic field is perpendicular to the current.[31] AMR was first discovered in the ferromagnetic (FM) metals Ni and Fe by William Thomson in 1856.[51] The AMR effect is defined as the difference between $\rho\|$ (resistivity when the magnetic moment M is parallel to the electric current i) and $\rho\perp$ (resistivity when M is perpendicular to i), defined as $\Delta\rho = \rho\| - \rho\perp$.

An increase in spin-dependent scattering causes the increase in AMR. Increasing magnetization also enhances the TMR because it results in increased spin polarization. AMR is not only influenced by temperature but also by lattice distortions caused by doping.[52]

The AMR effect is often observed in various types of thin films of ferromagnetic metals and alloys such as Fe, Co, and Ni.[53] The anisotropic resistance in Ni–Fe and Ni–Co alloys depends on the orientation of the magnetic moment related to the direction of the electric current arising from spin–orbit coupling. In Fig. 1D(i), it is shown that if M (magnetic moment perpendicular to i and spin–orbit parallel to i), the cross-sectional area for the resulting scattering is small, leading to low resistance. Conversely, in Fig. 1D(ii), if M is parallel to i and spin–orbit is perpendicular to i, the cross-sectional area for scattering is large, resulting in high a resistance.

3. Parameters that affect magnetoresistance

3.1 Magnetic parameters

With the application of a magnetic field, there is a decrease in resistivity, particularly under saturating magnetic fields. In Fig. 2A and B, the resistivity rapidly decreases, followed by a rapid increase in magnetization values. This is based on a double-exchange interaction mechanism. In this mechanism, the alignment of the Mn spin directions leads to an increased electrical conductivity. Conversely, it becomes difficult for electron transfer between ion difficult to cross domain walls in different magnetization directions, resulting in high resistivity. Under a strong magnetic field, the magnetic domains tended to align with the field direction. As a result, electrons can easily cross the domain-wall boundaries, leading to a decrease in resistivity and an increase in the MR value.[54] Magnetization increases owing to the rotation of the magnetic domains influenced by the magnetic field. Simultaneously, this causes a sharp decrease in the resistance, underpinning the negative MR values at high magnetic fields.[55] Furthermore, at decrease in ferromagnetic coercivity (H_c) occurs with an increase in grain size, indicating a transformation from a multi-domain state to a single-domain state in the ferromagnetic grains.[56]

3.2 Electrical parameters

Applying a magnetic field, significantly decreases the resistivity across the entire temperature range. The decrease in resistivity resulted in an increase in the MR value. In Fig. 2C and D with a 5 T magnetic field, the maximum MR value occurs at a temperature of 330 K, which is slightly lower than the peak resistivity at around 340 K. The MR experiences a slight increase as the temperature decreases. This indicates a correlation between the magnetization and resistivity of the material. Under the influence of a magnetic saturation field, the resistivity decreases significantly, whereas at fields above the saturation level, the resistance decreases more slowly than at low fields.[54] This is

Open Access Article. Published on 11 June 2024. Downloaded on 2/18/2026 10:19:39 AM.
This article is licensed under a Creative Commons Attribution-NonCommercial 3.0 Unported Licence.

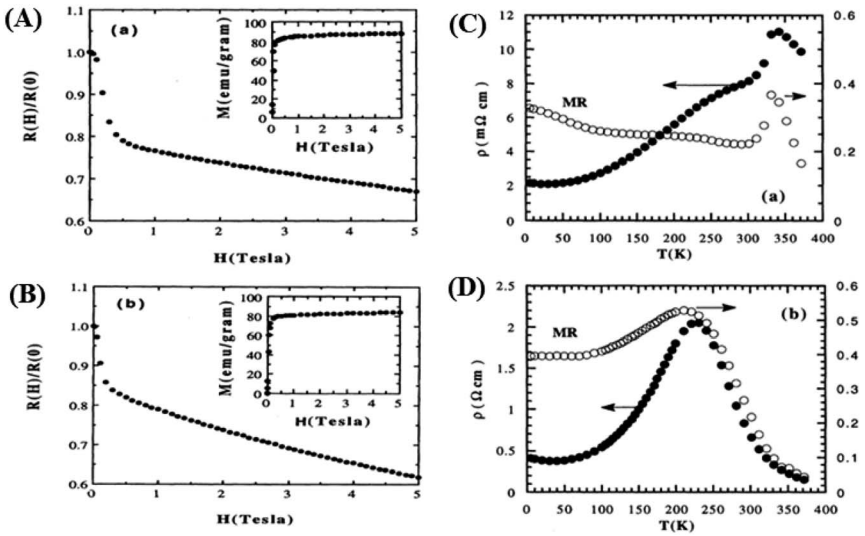

Fig. 2 [A] Field dependence of relative resistivity and magnetization at 5 K for, $La_{0.67}Ba_{0.33}MnO_{2.99}$ and [B] $La_{0.67}Ba_{0.33}MnO_{2.90}$). Reprinted with permission from the American Physical Society.[54] Curves of resistivity (filled circles) and MR ratio (empty circles) against temperature for [C] $La_{0.67}Ba_{0.33}MnO_{2.99}$ and [D] $La_{0.67}Ba_{0.33}MnO_{2.90}$. Reprinted with permission from the American Physical Society.[54]

because the magnetic field deflects the charge carriers (electrons) and aligns the magnetic spins in the manganite compound. Therefore, the resistivity decreases when electrons move under the influence of DE, causing a shift in the transition metal–insulator (T_{MI}) characteristics.[22]

4. Classification of magnetoresistance materials groups

4.1 Perovskite structure material (ABO_3)

Research on perovskite manganite materials has seen significant developments in the past few decades. Perovskite materials based on manganese oxide have the general formula $R_{1-x}A_xMnO_3$, where R is a rare earth element, and A is a divalent element (Fig. 3A). Doping manganese with other elements results in superior properties, with theoretical calculations indicating the presence of additional multiferroic magnetic phases.[57] Some manganite perovskite materials that show MR values include manganite perovskites based on $LaMnO_3$ ([46] and [58–60]) and $NdMnO_3$.[22]

Similar to the study by Mahesh *et al.*, that $La_{1-x}A_xMnO_3$ (A = Ca, Sr) exhibits a remarkably large negative magnetoresistance with a doping range of $0.2 \leq x \leq 0.5$. Dynamic or static Jahn–Teller effects plays a crucial role in explaining the colossal magnetoresistance (CMR) effect in perovskite materials such as manganese oxides.[61] The mixed valence state, between Mn^{3+} and Mn^{4+}, can be enhanced by the fractional substitution of La^{3+} sites with divalent alkaline earth ions, influencing the magnetic transition temperature in the system. This transition can be explained by the double exchange (DE) interaction between Mn^{3+} and Mn^{4+} ions. This affects the system in the MnO_6 octahedral, where ion doping causes distortion in the Mn–O plane, leading to significant changes in the structural and transport properties. $LaMnO_3$ perovskite exhibits a varied phase diagram owing to changes in electron behavior in the 3-d orbital. This behavior arises from the complex exchange involving charge, spin, orbital, and lattice degrees of freedom.[62] The undoped $LaMnO_3$ parent compound exhibited a different crystal structure. There are two phases at room temperature, distorted orthorhombic and trigonal. Atom substitution at specific sites can influence the vibrational properties of the base material based on bond strength, mass, and ionic radii. Notably the insulating state in $LaMnO_3$ changes, displaying metallic behavior at room temperature by adjusting the doping ratio. This indicates that the structural phase transition acts as a trigger for the metal–insulator transition.[63]

Manganite perovskite materials exhibit diverse properties, owing to their unique electromagnetic properties, such as interactions between the spin, charge, and orbitals.[7] The addition of doping is usually employed to control the spontaneous exchange bias (SEB) effect. For instance, partial substitution of Ba in $La_{1.5}Sr_{0.5-x}Ba_xCoMnO_6$ enhances the SEB effect. This effect can be further improved with concentrations of Sr or Ba, relating to changes in the balance between the crystal field and Coulomb repulsion acting on Co, affecting its spin state, leading Co to pair with Mn ions. The combination of Co and Mn becomes crucial for the spin state, and presence of the spin glass (SG) phase. When magnetic Co ions are substituted with non-magnetic Ga^{3+}, it weakens the spin interaction of CO^{+}–O^{2-}–Mn^{+} (ferromagnetic interaction) and generates other interactions such as Co^{3+}–O^{2-}–Co^{3+} (antiferromagnetic interaction), resulting in a decrease in Curie temperature (T_C).[8] In $La_{0.5}Sr_{0.5}FeO_{3-\delta}$ (LSFO), the material crystallizes in a perovskite structure because the substitution of Sr for La creates oxygen vacancies and electron holes to maintain electronegativity. In addition, the insertion of oxygen ions entering LSFO also lead to changes in the concentration of Fe^{3+} and oxygen vacancies. This results in a rapid oxygen diffusion rate and enhances the capacitance based on oxygen anions.[64]

© 2024 The Author(s). Published by the Royal Society of Chemistry

Open Access Article. Published on 11 June 2024. Downloaded on 2/18/2026 10:19:39 AM.
This article is licensed under a Creative Commons Attribution-NonCommercial 3.0 Unported Licence.

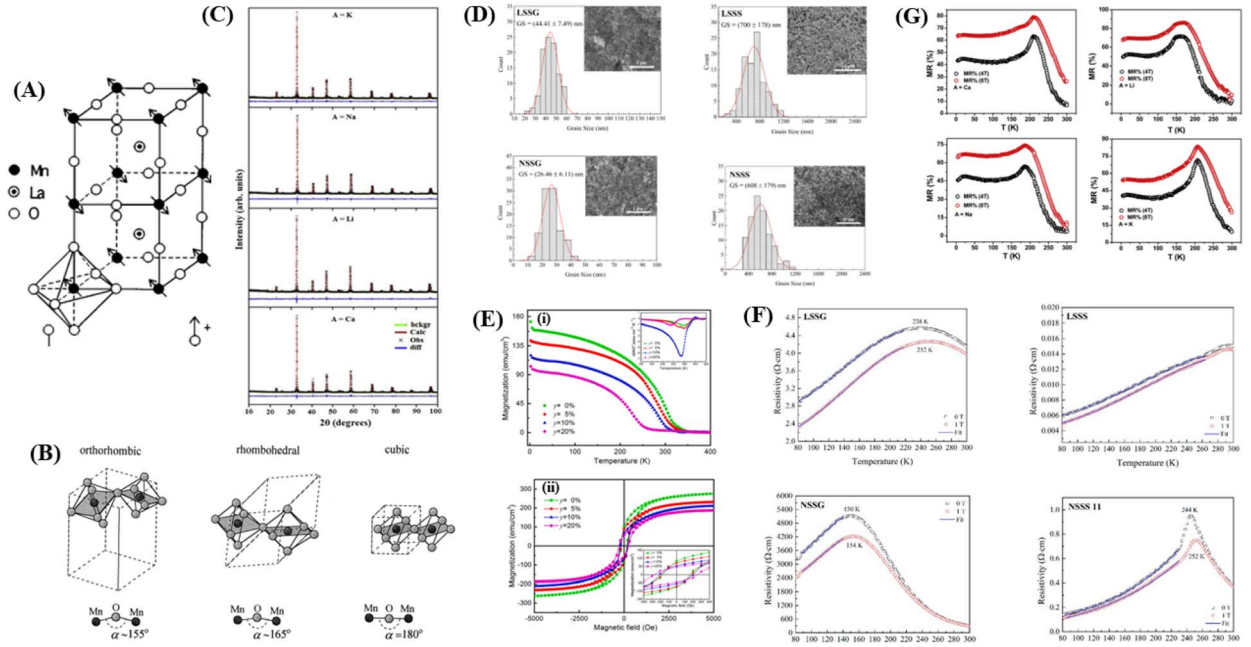

Fig. 3 [A] Perovskite structure $LaMnO_3$. Reprinted with permission from the American Physical Society.[147] [B] Schematic arrangement of octahedral MnO_6. Reprinted with permission from the Elsevier.[67] [C] Rietveld for XRD pattern of $La_{0.5}Nd_{0.15}Ca_{0.25}A_{0.1}MnO_3$). Reprinted with permission from the Elsevier.[148] [D] Grain size distribution histogram and FESEM micrographs of manganite samples (https://doi.org/10.3390/, Open source MDPI).[22] [E] (i) Magnetization *versus* temperature (500 Oe) of LSMZO film. The inset shows the temperature derivative of magnetization (d*M*/d*T*) curve. (ii) Hysteresis loop of LSMZO film recorded at 10 K Reprinted with permission from the Elsevier.[87] [F] shows the electrical resistivity as a function of temperature for LSMO and NSMO manganites under an applied magnetic field of 0 and 1 T).[22] [G] Plot of magnetoresistance (MR%) as a function of temperature (*T*) for $La_{0.5}Nd_{0.15}Ca_{0.25}A_{0.1}MnO_3$) (https://doi.org/10.3390/coatings11030361, open source MDPI).[22]

Numerous studies have been conducted on hole-doped manganite materials, showing complex phases of orbital/spin/charge, and ferromagnetic (FM) – antiferromagnetic (AFM) dependent on the doping percentage (x) and temperature, where x represents the concentration of Mn^{4+} ions or the percentage of doping of divalent atoms. In the antiferromagnetic insulator $LaMnO_3$ compound of type A, doping with divalent ions such as Ca, Sr, and Ba transforms its antiferromagnetic insulator properties into ferromagnetic metal by varying the ratio of Mn^{3+} and Mn^{4+}. It was found that at a doping concentration $x = 0.3$, the concentration of Mn^{4+} reached a level where the double exchange (DE) mechanism between Mn^{3+}–O–Mn^{4+} dominated the super exchange interaction between Mn^{3+}–O–Mn^{3+} and Mn^{4+}–O–Mn^{4+}. This indicates significant colossal magnetoresistance (CMR) in the Curie temperature (T_C) region.[65]

The following sections describe the crystal structure and morphology, electrical properties, magnetic properties, and MR of several perovskite materials.

4.1.1 Crystal structure. In perovskite-structured materials, based on the law of charge conservation, the $LaMnO_3$ perovskite material ($La^{3+}Mn^{3+}O_3{}^{2-}$) exhibits stable charges with an ideal cubic structure containing La^{3+}, Mn^{3+}, and O^{2-} ions. This oxidation state structure allows super exchange interaction to occur between Mn^{3+}–O^{2-}–Mn^{3+}. By substituting La^{3+} sites with divalent ions such as Ba^{2+}, Ca^{2+}, and Sr^{2+}, a new stability is formed, $La^{3+}{}_{1-x}\,AE_x{}^{2+}Mn_{1-x}{}^{3+}\,Mn_x{}^{4+}$. This new stability results in the mixed valence of Mn^{3+} and Mn^{4+}, leading to double exchange (DE) interactions. Substitution at La^{3+} sites with divalent ions also distorts the structure owing to differences in the radii of La^{3+} and divalent ions.[66] In the perovskite material LSMO ($La_{0.7}Sr_{0.3}MnO_3$), there are two types of crystal structures, namely rhombohedral ($R3c$) and orthorhombic ($Pbnm$), depending on the temperature and chemical composition. Both structures have distorted MnO_6 octahedra, possibly owing to lattice mismatch with the substrate material.[67]

From Fig. 3B, it is evident that there are distortions and structural changes in LSMO that are highly dependent on the concentration and radii of the substituting ions. Fig. 3B, also shows that the MnO_6 octahedral bonds undergo distortion, indicating a change in the bond lengths of the Mn–O–Mn ions. According to the Double Exchange (DE) theory, changes in $d\langle$Mn–O$\rangle$ and $\langle$Mn–O–Mn$\rangle$ influence the bandwidth (W). A decrease in W weakens the DE interaction between Mn^{3+}–O–Mn^{4+} owing to a reduction in electron mobility caused by an increase in the $d\langle$Mn–O$\rangle$ length and a decrease in the $\langle$Mn–O–Mn$\rangle$ angle. Here, W is determined using the equation:[68]

$$W = \frac{\cos\frac{1}{2}(\pi - \langle \mathrm{Mn-O-Mn}\rangle)}{d_{\langle \mathrm{Mn-O}\rangle}{}^{3.5}} \quad (1)$$

As an example, the X-ray diffraction (XRD) results of the perovskite material (LMO) with the composition

Open Access Article. Published on 11 June 2024. Downloaded on 2/18/2026 10:19:39 AM. This article is licensed under a Creative Commons Attribution-NonCommercial 3.0 Unported Licence.

$La_{0.5}Nd_{0.15}Ca_{0.25}A_{0.1}MnO_3$, where (A = Ca, Li, Na, and K), as shown in Fig. 3C using the solid-state reaction method, revealed that the material has an orthorhombic crystal structure in the *Pbnm* space group. In Fig. 3C, sharp and intense peaks are observed, consistent with the perovskite structure, indicating good sample crystallinity with no detected secondary phases. Different ion substitutions (Ca, Li, Na, and K) lead to changes in the unit cell volume of the material. With Na ion substitution, the unit cell volume decreased, whereas samples substituted with K ions showed a significant increase. This is because the average ionic radius of Na^+ is smaller than that of Ca^+ and K^+ ions. The average size of crystals is determined using the Scherrer equation as follows:

$$\mathrm{Ds} = \frac{K\lambda}{\beta_{hkl}\cos\theta} \quad (2)$$

where $K = 0.9$, which is a constant corresponding to the crystallinity factor, λ is the XRD wavelength, β_{hkl} is the full width of half maximum (FWHM) at the maximum intensity peak, and θ is the diffraction angle.[68]

When the ionic radii of the dopant atoms at the A sites increase, the internal pressure decreases, reducing the distortion of the MnO_6 octahedra. This increases the Mn–O–Mn angle, lattice parameter, and unit cell volume. The increase in the unit cell volume causes a decrease in the density owing to the increased molecular mass. As the radius of A increases, there is a decrease in the Mn–O bond length. An increase in the Mn–O–Mn bond angle compensates for the reduction in Mn–O bond length. This is because the spaces in the cell are filled with larger-radius A-site cations, and the increased compressive stress shortens the Mn–O–Mn bond in the MnO_6 octahedra, which is related to the Mn–O–Mn and Mn–O bond lengths. The level of distortion in the unit cell structure was measured by the Goldschmidt tolerance factor (t) using the following equation:

$$t = \frac{1}{\sqrt{2}}\frac{[r_A - r_O]}{[r_B - r_O]}. \quad (3)$$

where $\langle r_A\rangle$,$\langle r_B\rangle$, and $\langle r_O\rangle$ are the average ionic radii of ions A, B, and O in the ABO_3 perovskite structure. If the equilibrium bond lengths of A–O and B–O match perfectly at $t = 1$, the structure is an ideal cubic perovskite structure. If $t < 1$, the B–O bonds are under tension, and the A–O bonds are under compression. Thus, internal stresses arise in the structure, canceling each other out, indicating cooperative distortion of the MnO_6 octahedra, which reduces the structural symmetry. For $t < 0.96$, the material has an orthorhombic structure, and for $0.96 < t < 1$, the structure is rhombohedral.[69] With the influence of doping, t approaches 1 as $\langle r_A\rangle$ increases because the structural distortion decreases. The broadening of the peaks is a result of lattice strain owing to the presence of subgrain dislocations and distortions. The pressure within the lattice is divided into micro and macro pressures, where the micro pressure varies within the grain, whereas macro pressure is constant over long distances. Similarly, the strain in a crystal can be either uniform or non-uniform. Uniform tensile strain results in a peak shift toward lower angles, whereas non-uniform strain caused grain bending and widens the diffraction peaks. The broadening of the diffraction peaks is caused by crystal imperfections and distortions.[65]

The tolerance factor is a term related to the bond-length mismatch of the A–O and B–O bonds, which are associated with the ionic radii. Distortions tend to disappear at high temperatures because of the greater thermal expansion of the A–O bond lengths. When $t > 1$, the A–O bonds undergo compressed, whereas the B–O bonds are under tension.[70] The influence of the tolerance factor is a major factor affecting the magnetic properties of materials, such as affecting T_C and T_ρ. This is related to the DE interaction, which was influenced by the ratio of Mn^{3+} to Mn^{4+}. A stronger DE results in a higher T_ρ. There are three factors that greatly affect T_ρ, including the hole carrier density controlled by the ratio $[Mn^{3+}]/[Mn^{4+}]$, $[r_A]$, and cation mismatch (σ^2) determined by the equation:

$$\sigma^2 = \sum y_i r_i^2 - \langle r_A\rangle^2 \quad (4)$$

where $y_i(\sum y_i = 1)$ is the fractional occupancy and r_i is the variation in the cation radius at site A.[71–73] An increase in $\langle r_A\rangle$ strengthens DE because of the increase in the one-electron e_g band.[74] According to Thanh *et al.*, T_C increases in manganite materials during the rhombohedral–orthorhombic phase transition. T_C decreases with the dispersion of the A-cation radius σ^2. The cation mismatch (σ^2) becomes a key factor affecting the T_C of perovskite manganites. T_C decreases owing to the influence of the average size of the A-site cations. The substitution of cations with different radii leads to irregularities in the ion sizes. Structural irregularities result in local strain within the MnO_6 octahedral bonds and affect the Mn–O–Mn angle, which in turn leads to changes in the lattice parameters and magnetic properties. The lattice distortion becomes pronounced and provides a local trap for e_g electrons. Additionally, it causes the hopping amplitude of the charge carriers between Mn^{3+} and Mn^{4+} to decrease because the Mn–O–Mn angle decreases (<180°), resulting in distortion of the MnO_6 octahedral lattice. Consequently, the mobility of the carriers decreases as the charge localization tendency increases. This results in a decrease in T_ρ.[75] The influence of substitution on T_C and T_ρ can be understood by analyzing the size mismatch (σ^2) on the A-site cations, which indicates oxygen displacement or local strain in manganite materials.[76] The increasing irregularity in the size of the radii leads to a monotonic decrease in the ferromagnetic-paramagnetic transition temperature, which is significantly correlated with the CMR. This decrease in T_C was caused by the formation of microscopic and mesoscopic phases at the grain boundaries.[73]

4.1.2 Morphological structure. The synthesis method and the sintering temperature influence grain size of perovskite materials. For instance, Lau *et al.*, the materials $La_{0.7}Sr_{0.3}MnO_3$ and $Nd_{0.7}Sr_{0.3}MnO_3$ using two different methods: the sol–gel (SG) method and the solid-state reaction (SS) method. From the grain size distribution histograms and FESEM micrographs in Fig. 3D, all samples exhibited a uniform grain size distribution consisting of irregularly shaped grains. In the solid-state reaction method, where the samples were heated at a higher temperature (1100 °C), the solid-state samples (LSSS and NSSS)

© 2024 The Author(s). Published by the Royal Society of Chemistry

Open Access Article. Published on 11 June 2024. Downloaded on 2/18/2026 10:19:39 AM. This article is licensed under a Creative Commons Attribution-NonCommercial 3.0 Unported Licence.

exhibited a more compact and denser morphology than the sol–gel samples (LSSG and NSSG), which were sintered at a lower temperature. The solid-state method produces grains in the submicron size range (608–7000 nm), whereas the sol–gel samples yield grain sizes in the nanometer range (26–45 nm).[22] The grains consist of several crystallites arranged in the same orientation. The grain and crystallite sizes increased with the sintering temperature owing to the congregation effect.[77] However, single crystallite grains can form when the sample is sintered at low temperatures.[78]

In study by Munazat *et al.*,[79] the material $La_{0.7}Ba_{0.1}Ca_{0.1}Sr_{0.1}MnO_3$, synthesized using the sol–gel and wet mixing (WM) methods, showed that the grain size of the MW sample was smaller than that of the SG sample. This is evidenced by the XRD and SEM results indicating that the crystallite and grain size of WM are smaller than those of SG. Both the samples were subjected to the same heat treatment. This difference can be attributed to the SG method being carried out under neutral pH conditions, whereas the WM method was performed under acidic conditions because of the precursor was dissolved in nitric acid. This indicates that pH and the use of a chelating agent are important parameters that influence the resulting grain size. In perovskite synthesis, the grain size is influenced by chemical reactions under pH conditions.[80]

In a study by Das *et al.*, it wass also stated that grain growth increases with increasing sintering temperature, leading to a reduction in grain boundaries. The effect of sintering temperature on grain size showed a similar influence on the XRD results. Significant differences in grain shape were observed by synthesizing $CoFe_2O_4$ materials with varying the sintering temperature from 300 °C to 1200 °C, grain shapes such as spheres ($T = 300$ °C), pyramids (CFO – 450 °C), ($T = 600$ °C), lamellae ($T = 750$ °C), octahedra ($T = 900$ °C), and truncated octahedra ($T = 1200$ °C) were observed, with uniform grain shapes in all samples. It is estimated that different grain shapes have a significantly impact on the material's physical properties.[81] The increase in grain size because of the temperature rise is caused by the coalescence of crystallites at higher temperatures.[82] By increasing the sintering temperature, the grains were enlarged and the porosity was gradually reduced. The porosity of materials can lead to crystallographic defects and significantly affect the material's physical properties.[83]

4.1.3 Magnetic properties. In a study by Joseph *et al.*, it was reported that the magnetization curve of the perovskite material ($La_{0.833}K_{0.167}MnO_3$) shows that below the critical temperature (T_c), the material exhibits ferromagnetic behavior and shows rapid saturation under the influence of a low magnetic field, indicating faster domain wall motion because of shorter relaxation times in this compound. The magnetization values decreased as the temperature increases. This is attributed to magnetic inhomogeneities which may be related to phase separation between La^{3+} and monovalent K^+ ions. For each K^+ substitution at the La^{3+} site, twice the amount of Mn^{3+} ions are oxidized to Mn^{4+}, resulting in an excess of Mn^{3+} regions around La^{3+} and excess Mn^{4+} regions around K^+ ions. Because of this inhomogeneity, the ground state of the compound is influenced by various interactions, including ferromagnetic (FM) interactions between Mn^{3+}–Mn^{4+} ions from double exchange (DE) interactions, and antiferromagnetic (AFM) interactions between Mn^{3+}–Mn^{3+} and Mn^{4+}–Mn^{4+} ions from super exchange (SE) interactions. The coexistence of these interactions results in random spin orientations, and reduce magnetization at high temperatures.[59] The magnetization curve of perovskite materials shows an increase with the external magnetic field and decreases with an increasing temperature.[19–78,80–86] In research by Yin *et al.*, Fig. 3E(i) shows $La_{0.9}Sr_{0.1}Mn_{1-y}Zn_yO_3$ ($y = 0\%$, 5%, 10%, and 20%) materials revealed a magnetization–temperature (M–T) curve showing a ferromagnetic–paramagnetic (FM–PM) phase transition at a magnetic field of 500 Oe at T_c, where T_c is defined as dM/dT. The curve indicates a decrease in T_c and an increase in magnetization with an increase Zn content. This occurs because of a decrease in DE interaction and an increase in electron-lattice coupling. The hysteresis loop shows saturation above 25 000 Oe, and there is a decrease in the saturation magnetization (M_s) and an increase in coercive field (H_c) with increasing Zn content (Fig. 3E(ii)). H_c depends heavily on the microstructure of the ferromagnetic material, such as structural mismatches and defects that affect the magnetic domains. Substitution of Zn^{2+} ions can induce internal strain at Mn sites because of the large ionic radius mismatch between Zn^{2+} and Mn^{3+}/Mn^{4+}, resulting in lattice distortion, including the rotation of MnO_6 octahedra and a decrease in Mn–O distance and Mn–O–Mn angle. Doping also distorts of the Mn–O–Mn angle, making it smaller, and increasing the Mn–O distance distribution. This suggests that increasing mismatch in the substituted cation size leads to a decrease in T_c, as well as metal–isolator transition temperature in perovskite manganites.[87]

4.1.4 Electrical properties. Most perovskite manganites behave as insulators (paramagnetic) above the T_{MI} temperature, as evidenced by decreased in resistivity at temperatures above the T_{MI}. At temperatures below T_{MI}, the material behaves as a metal (ferromagnetic), as evidenced by an increase in resistivity with increasing temperature below the T_{MI} temperature.[76] The increase in resistivity reached a maximum peak at the metal–insulator transition temperature (T_{MI}). The electrical resistivity is influenced by grains and grain boundaries, as both act as scattering regions for electron transport.[88] In Fig. 3F, the resistivity *vs.* temperature (ρ *vs.* T) is depicted for $La_{0.7}Sr_{0.3}MnO_3$ and $Nd_{0.7}Sr_{0.3}MnO_3$ samples under magnetic field of 0 and 1 T. The resistivity in the $Nd_{0.7}Sr_{0.3}MnO_3$ sample is significantly higher than that of $La_{0.7}Sr_{0.3}MnO_3$ because of its larger band gap and lower electron mobility than. Additionally, there was a difference in resistivity values between samples produced by the SG and SS methods. Nanocrystalline materials exhibit a higher resistivity than submicron materials. This increase in resistivity can be associated with the enhancement of grain boundaries in nano-sized materials. Grain boundaries act as potential barriers, localization electrons on Mn.[40] T_{MI} in $Nd_{0.7}Sr_{0.3}MnO_3$ with nano-sized grains occurred at a lower temperature range. This is attributed to the increased scattering of charge carriers owing to higher magnetic disorder at the grain boundaries of nano-sized materials. The enhanced grain boundaries in nano-sized grains can also reduce the DE interaction between Mn^{3+} and Mn^{4+}, leading to an increase in

Open Access Article. Published on 11 June 2024. Downloaded on 2/18/2026 10:19:39 AM. This article is licensed under a Creative Commons Attribution-NonCommercial 3.0 Unported Licence.

resistivity. Furthermore, the decrease in DE interaction is caused by the increase in the Mn–O bond length and the decrease in the Mn–O–Mn angle, reducing the bandwidth and electron mobility. In Fig. 3F, T_{MI} also shifts towards higher temperatures by applying of a magnetic field. This is because the magnetic field displaces charge carriers (electrons in Mn atoms) and aligns the magnetic spins in the manganite compound. Therefore, resistivity decreased as electrons moved under the influence of DE, resulting in a shift in the T_{MI}.

4.1.5 Magnetoresistance (MR) properties. MR is classified into two types based on different origins: intrinsic CMR and extrinsic CMR. Intrinsic MR depends only on temperature, whereas extrinsic MR is related to grain boundaries and generally occurs at low temperatures. Intrinsic MR increases near the *I–M* transition temperature.[89] Intrinsic MR is explained by the DE mechanism and the Jahn–Teller effect. However, in polycrystalline manganites, MR values are observed over a wide temperature range, which is considered an extrinsic MR effect. The extrinsic MR is influenced by spin-polarized tunneling between neighboring ferromagnetic grains and spin-dependent scattering. This type of MR can be enhanced by controlling the grain boundaries substituting of divalent ions at the A-site of manganites.[90] External MR is also commonly found in thin films, typically requiring only low magnetic field application, and peaking at temperatures below T_c. Extrinsic MR is influenced by spin-polarized tunneling at the grain boundaries.[91]

The magnetoresistance (MR) properties of perovskite materials are highly interesting, leading to investigations regarding MR determined by the decrease in the electrical resistivity of the material under the influence of an external magnetic field. The strong MR effect results from the coexistence of ferromagnetism and metallic conductivity. The percentage of magnetoresistance is defined as % MR = $(\rho 0 - \rho(H))/\rho 0 \times 100\%$, where $\rho(0)$ is the resistivity at zero field and $\rho(H)$ is the resistivity under an applied magnetic field. In the study by Kumar *et al.*, the %MR values for $La_{0.5}Nd_{0.15}Ca_{0.25}A_{0.1}MnO_3$ (A = Ca, Li, Na, and K) in Fig. 3G were found to be 80%, 87%, 75%, and 84% for samples doped with Ca, Li, Na, and K at the TMS with the application of an 8 T magnetic field. The highest magnetoresistive effect observed around TMS is attributed to the increased ferromagnetic interaction because of the alignment of parallel spins in the Mn–O–Mn coupling. Additionally, significant MR effect was observed at low temperatures, which could be attributed to the influence of carrier scattering at the grain boundaries.[92] When electrons move from one grain to another, they encounter insulation barriers between grains, and each can scatter the electrons because of the reduced connectivity between the grains or surface contamination. A strong magnetic field can overcome strong electron scattering, resulting in high magnetoresistance at low temperatures.[93]

The external CMR is related to grain boundaries, which can be explained by spin-polarized tunneling and spin-dependent scattering. Many efforts have been made to enhance CMR in materials, one of which is creating manganite composite materials with have a secondary phase as an insulator. Several studies have reported an increase in MR values.[43,94,95] Additionally, vacancy substitution in manganite materials can also enhance the MR value.[96,97]

4.2 Alloy

Several alloy groups that show the phenomenon of MR, including Ni–Mn based,[98] Co–Fe,[50] and Ni–Cu.[99] In Ni–Mn–Z-based alloys, the magnetic moment (ΔM) can be significantly enhanced by the addition of a fourth element, composition adjustment, and heat treatment. Specifically, doping with Fe/Co atoms can act as a "ferromagnetic activator" inducing the alignment of magnetic moments (of Mn–Mn nearest neighbors), resulting in ferromagnetic behavior and creating a strong magnetostructural coupling state. For instance, in the study conducted by Zhang *et al.*, the $Ni_{41}Mn_{43}Sn_{10}Co_6$ alloy showed a ΔM value of 90 A m^2 kg^{-1} under the influence of a 5.0 T magnetic field, which is significantly larger than that of the $Ni_{47}Mn_{43}Sn_{10}$ alloy without Co doping ($\Delta M = \sim$16 A m^2 kg^{-1})[17] In addition, ΔM was found to experience a significant increase with the substitution of Ni by 4.2% with Fe in the $Ni_{50}Mn_{38.0}Sn_{12.0}$ alloy, specifically from 16 A m^2 kg^{-1} to 58 A m^2 kg^{-1}.[100] However, the magnetocaloric effect (MCE) associated with the first-order martensitic transformation characterized by a large isothermal magnetic entropy change (ΔSM) shows a narrow operating temperature range of approximately 1–5 K, which poses a barrier to the practical application of this alloy for magnetic refrigeration. To expand the operating temperature range with refrigeration capacity (RC), strategies such as reducing the material size (thin films or microwires) need to be implemented.[101] In the study by Zhang *et al.*, using the material $Ni_{46.8}Mn_{38.1}Sn_{11.6}Fe_{3.5}$, the highest negative magnetoresistance (MR) values were observed, reaching 40.8% at 261 K and 26.7% at 275 K during the cooling and heating processes.[102]

The following sections describe the crystal structure and morphology, electrical properties, magnetic properties, and MR of several alloy materials.

4.2.1 Crystal structure. Several X-ray diffraction (XRD) results from the alloy material are as follows: the $Ni_{43}Mn_{41}Co_5Sn_{11}$ alloy exhibited a cubic L21 phase with a structure (space group *Fm*3*m*) in the austenitic phase.[103] The Ni_2MnSn alloy exhibits a face-centered cubic (FCC) structure.[102] The $Mn_{1.9}Co_{0.1}Sb$ alloy exhibited a tetragonal structure with the space group *P*4/*nmm*,[104] and the $Ni_{45}Mn_{43}CrSn_{11}$ alloy exhibits a cubic structure.[105]

In Fig. 4A, it can be observed that a single phase in the $Mn_{1.9}Co_{0.1}Sb$ alloy is obtained after substituting Co with a tetragonal Cu_2Sb structure (space group *P*4/*nmm*) with lattice parameters a = 4.1048 Å and c = 6.4770 Å, obtained from Rietveld refinement. The unit cell volumes whereas V = 109.137 Å, and c/a = 1.577. The lattice parameters for the Mn_2Sb alloy were a = 4.07 Å and c = 6.54 Å. The results indicate that substituting Co is increase the lattice parameter a and decreasing c in the $Mn_{1.9}Co_{0.1}Sb$ alloy. There was a decrease in c/a by 1.8%, an increase in volume by 0.7%, and a contradictory change in a and c, suggesting anisotropic deformation of the crystal lattice in the Co-substituted Mn_2Sb alloy.

Furthermore, there are alloys with Heusler structures that have the composition X_2YZ, where X and Y are transition metal elements, and Z is an sp-element. The main group element Z occupies four different crystal locations, namely A (0, 0, 0), B (0.25, 0.25, 0.25), C (0.5, 0.5, 0.5), and D (0.75, 0.75, 0.75),

© 2024 The Author(s). Published by the Royal Society of Chemistry

Open Access Article. Published on 11 June 2024. Downloaded on 2/18/2026 10:19:39 AM.
This article is licensed under a Creative Commons Attribution-NonCommercial 3.0 Unported Licence.

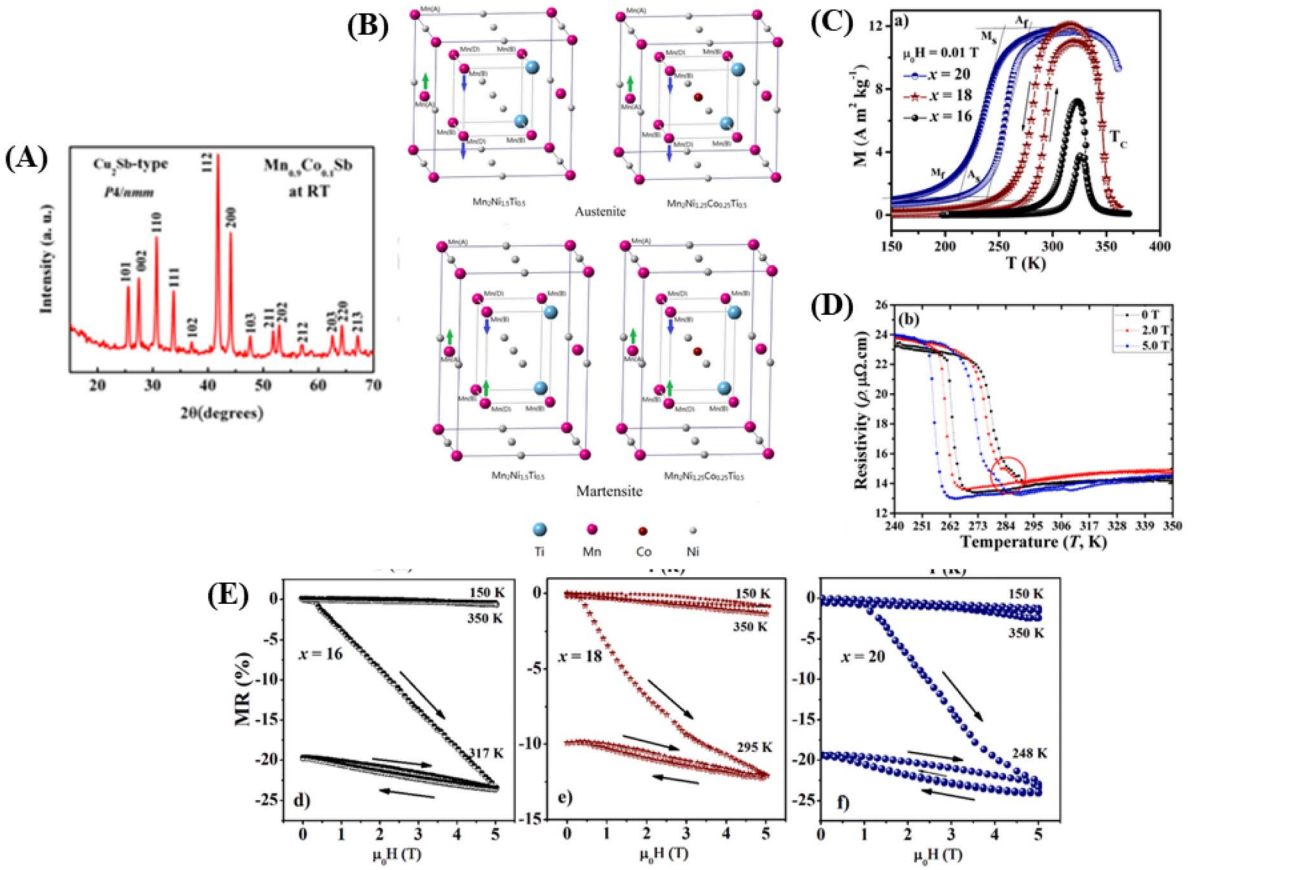

Fig. 4 [A] XRD pattern for $Mn_{1.9}Co_{0.1}Sb$ alloy at room temperature. Reprinted with permission from the AIP Publishing,[104] [B] Heusler alloy supercell model $Mn_2Ni_{1.5}Ti_{0.5}$ and $Mn_2Ni_{1.25}Co_{0.25}Ti_{0.5}$) Reprinted with permission from the Elsevier.[116] [C] M–T curve for alloys $Ni_{50-x}(FeCo)_x$-$Mn_{37}Ti_{13}$ (x = 16, 18 and 20) with 0.01 T). Reprinted with permission from the Elsevier.[98] [D] Electrical resistance curve (ρ–T) with respect to material temperature $Ni_{43}Mn_{41}Co_5Sn_{11}$ at 0, 2.0 and 5.0 T). Reprinted with permission from the Elsevier.[102] [E] MR is field-dependent throughout the martensite phase respectively, the magneto-structural transition of temperature and the austenite phase, respectively to x = 16, 18, 20 sampel. Reprinted with permission from the Elsevier.[98]

resulting in an ordered structure. An example of a Heusler alloy was found in the study by Ma *et al.*, where the material Mn_{50}-$Ni_{50-x}Ti_x$ had a cubic structure, and the Ni atoms enter the Mn site (C). This is based on the "valence electron counting rule" in Heusler alloys, which states that transition metal atoms with more valence electrons prefer to occupy A and C sites.[106] Crystal structures of Heusler alloys can be classified into two types: half (or semi-) with the chemical formula XYZ and full Heusler with the formula X_2YZ, where X and Y are transition metal elements and Z is an sp-element. In Full-Heusler compound system, when the valence of X is larger than Y, the atomic sequence becomes X–Y–X–Z along the diagonal direction of the cubic cell, and its structure is more commonly known as $L2_1$. However, when the valence of Y is the largest, the atomic sequence becomes X–X–Y–Z, known as the inverse-Heusler alloy.[107] Heusler alloys (HA) have become interesting materials for development owing to several advantages, including high Curie temperature (T_C), half metallicity, shape memory effect, thermoelectric properties, and ferromagnetism.[108–111] Owing to these advantages, HA is widely applied as spin filter, GMR materials, tunnel junctions, transducers, energy technology, spin valve, memory device, multiferroic, and for magnetocaloric effect. HAs have a large thermoelectric coefficient, which allows them to efficiently convert heat energy into electrical energy.[112,113]

A supercell model of a Heusler alloy is depicted in Fig. 4B, specifically for the materials $Mn_2Ni_{1.5}Ti_{0.5}$ and $Mn_2Ni_{1.25}$-$Co_{0.25}Ti_{0.5}$. The arrows on the Mn atoms indicate the sequence of spin moments. In the austenitic state, it behaves as ferromagnetic (FM), whereas in the martensitic state, it behaves as an antiferromagnetic (AFM).[114]

4.2.2 Magnetic properties. In the study by Samanta *et al.*, data (M–T curves) for the alloy material ($Ni_{50-x}(FeCo)_xMn_{37}Ti_{13}$) with ($x$ = 16, 18, and 20) were presented under the influence of an external magnetic field of 0.01 T under both zero-field cooled (ZFC) and field cooled (FC) conditions. The curves indicate that all samples exhibit the phase transition from paramagnetic (PM) to ferromagnetic (FM) at their respective Curie temperatures (T_C), followed by the martensitic transformation (MST) from the strong FM austenitic phase to the magnetic martensitic phase during cooling. The presence of thermal hysteresis in the M–T curves suggests that the MST is a first-order phase

Open Access Article. Published on 11 June 2024. Downloaded on 2/18/2026 10:19:39 AM. This article is licensed under a Creative Commons Attribution-NonCommercial 3.0 Unported Licence.

transition. The separation between the ZFC and FC curves at low temperatures indicates the presence of nonhomogeneous magnetic states in the system. The key features of the first-order phase transition temperatures include the martensite–austenite transition (TA = (As + Af)/2, where As is austenite start, and Af is austenite finish) and the austenite–martensite transition (TM = (Ms + Mf)/2, where Ms is martensite start, and Mf is martensite finish.[98] Fig. 4C indicates that with an increase in the value of x, both martensite start temperature (TM) and austenite start temperature (TA) shift towards lower temperatures, whereas T_C (Curie temperature) shifts towards higher temperatures. Generally, the valence electron concentration (the ratio of electrons to atoms, e/a) is related to the ratio of $\frac{TM}{TA}$.[115] The e/a ratio was found to decrease with the content of $(FeCo)_x$, as indicated by the TM/TA shifting towards lower temperatures. In the Ni–Mn–Ti system, Mn occupies the Ti site in the D position with antiferromagnetic (AFM) coupling with Mn at the B site, which is nearest to the austenitic and martensitic phases.[116] In this material, Co–Fe acts as an "FM activator" and transforms Mn (B)–Mn (D) AFM into Mn (B)–Fe/Co (A, C)–Mn (D) with ferromagnetic exchange coupling in the Heusler alloy system (A (0,0,0), B $(\frac{1}{4}, \frac{1}{4}, \frac{1}{4})$, C $(\frac{1}{2}, \frac{1}{2}, \frac{1}{2})$, D $(\frac{3}{4}, \frac{3}{4}, \frac{3}{4})$). It has also been reported that Co doping has a more significant effect on increasing FM exchange than Fe doping, but it increases hysteresis loss. Therefore, simultaneous Fe–Co substitution results in higher FM exchange interactions, decreased TM, and increased hysteresis T_C.[117]

4.2.3 Electrical properties. In Ni–Mn-based alloys, resistance of the parent phase exhibits semimetal behavior, whereas for the martensitic state, there is a sharp drop during the martensite transformation (MT). This was investigated using a four-probe method at 0.2 and 5.0 T. In the graph, a sharp decrease in resistance is observed corresponding to the MT, followed by a slow decrease as the temperature approaches martensite finish temperature, and then a nearly linear increase during the advancement (Af) of the MT owing to the presence of the intermartensitic phase. The MT process is highly dependent on the heat flow temperature as well as the magnetic and electrical resistance behaviors.[102] In the study by Ma *et al.*, during heating, the resistivity in the $Ni_{43}Mn_{41}Co_5Sn_{11}$ alloy in Fig. 4D initially shows a slight decrease with increasing temperature. The resistivity of the martensitic state exhibits behavior similar to that of a semimetal.[118]

4.2.4 Magnetoresistance (MR) properties. In Ni–Mn-based Heusler alloys ($Ni_{50-x}(FeCo)_xMn_{37}Ti_{13}$, where x = 16, 18, and 20), during cooling, twin boundaries undergo an increase and a change in lattice symmetry during martensitic transformation (MT) during cooling, thereby enhancing electron–phonon scattering.[114] Additionally, the superzone boundary gap can alter the density of electronic states near the Fermi surface, leading to an increase in resistivity because of electron spin scattering.[119] In Fig. 4E, it is shown that in the full martensitic region, at 150 K, the magnetoresistance (MR) values are very small, indicating that the transition to austenite cannot be accomplished. By increasing the magnetic field, the MR during the martensitic transition, at 370 K for x = 16, increases almost linearly and reached a maximum of 25.4% at 5 T. Meanwhereas, for x = 18 and x = 20 samples, near the MT (martensitic transition) at 295 K and 248 K, respectively, MR increases almost linearly for fields up to 3 T and 3.5 T, reaching 12.9% and 24% at 5 T. This is associated with the presence of additional Zeeman energy that overcomes the friction of twin boundary motion, and subsequently, some martensite transforms into the austenitic phase, resulting in significant MR.[120]

4.3 Spinel material

Materials with a spinel structure formulated as AB_2X_4 (Fig. 5A) exhibit interesting ground states associated with the interactions of charge, spin, and orbital degrees of freedom, strongly coupled with the lattice. In the B-sublattice, complexity arises owing to the competition between direct nearest neighbor (NN) and ferromagnetic (FM) interactions and exchanges between next-nearest neighbors (NNN), and antiferromagnetic (AFM) interactions. Therefore, the FM and AFM states depend on the separation of B sites.[10] As an example, compounds based on chromium (Cr) with the formula ACr_2X_4 (where A represents a transition metal and X includes the elements S, Se, or Te) various of physical properties. These properties arise from the complex interplay between structural, spin, charge, and orbital degrees of freedom.[12] In this spinel structure, the FM state arises from the superexchange (SE) interactions between 3d electrons of Cr ions mediated by oxygen. The exchange interaction between s and d electrons results in substantial spin in the electronic band. The dependence on the strength of spin–orbit coupling and exchange separation leads to spinel materials exhibiting magnetic semiconductor behavior.

Chromium-based compounds, represented as ACr_2X_4 (where A represents a transition metal and X represents S, Se, or Te), are currently of significant interest owing to their diverse physical properties. The physical properties of these materials arise from the complex interplay between their structure, spin, charge, and orbital degrees of freedom. For example, $CuCr_4X_4$ is a metal, $CdCr_2Se_4$ is a semiconductor, $HgCr_2Se_4$ (n-type) is a semi-metal showing ferromagnetic behavior, $MnCr_2Se_4$ a semiconductor with ferromagnetic properties, and $ZnCr_2S_4$ is an insulator with antiferromagnetic characteristics. Some of these materials are of interest because of their ferromagnetic ordering and the emergence of semimetallicity predicted by band structure calculations. The FM order arises from the superexchange (SE) interaction between the 3d electrons of Cr ions mediated by anions. The SE interaction between s and d electrons results in substantial spin splitting from the electronic band. This is dependent on the strength of spin–orbit coupling and exchange splitting. Sayyan *et al.* reported that $FeCr_3Te_4$ underwent a ferrimagnetic (FIM) transition at a critical temperature (T_c) of 123 K. This result indicates that the FIM interaction in $FeCr_2Te_4$ emerges because of the FM interaction between antiferromagnetic Cr–Fe–Cr layers being magnetically coupled. This compound also exhibits Hall effect anomalies at temperatures <123 K, primarily dominated by the extrinsic skew-scattering mechanism rather than intrinsic Karpus–Luttinger or extrinsic hopping mechanisms.[12]

© 2024 The Author(s). Published by the Royal Society of Chemistry

Open Access Article. Published on 11 June 2024. Downloaded on 2/18/2026 10:19:39 AM. This article is licensed under a Creative Commons Attribution-NonCommercial 3.0 Unported Licence.

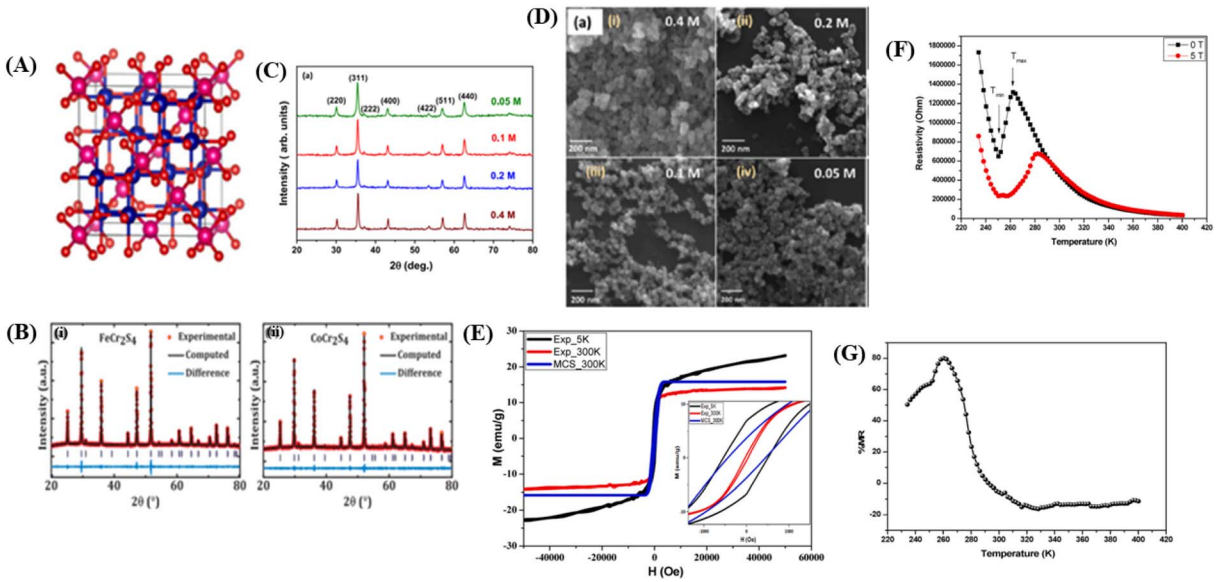

Fig. 5 [A] The crystal structure of the spinel. Reprinted with permission from the Elsevier.[11] [B] Rietveld refinement of powder X-ray diffraction pattern (i) $FeCr_2S_4$ and (ii) $CoCr_2S_4$. Reprinted with permission from the Elsevier.[121] [C] X-ray diffraction data of Fe_3O_4 nanoparticles prepared using different concentrations of precursor). Reprinted with permission from the Elsevier.[122] [D] FESEM images showing the surface morphology of Fe_3O_4 nanoparticles prepared from different precursor concentrations). Reprinted with permission from the Elsevier.[122] [E] Experimental and theoretical magnetic hysteresis circles of $SnFe_2O_4$ nanoparticles). Reprinted with permission from the Elsevier.[11] [F] Dependence of electrical resistivity of $SnFe_2O_4$ on temperature under different magnetic fields. Reprinted with permission from the Elsevier.[11] [G] Magnetoresistance *versus* temperature for $SnFe_2O_4$ nanoparticles. Reprinted with permission from the Elsevier.[11]

The following is a presentation of the crystal structure and morphology, electrical properties, magnetic properties, and MR of several spinel materials.

4.3.1 Crystal structure. The XRD characterization results for several spinel materials indicated that these substances had a single phase with a cubic spinel structure within the $Fm\bar{3}m$ space group. For example, in the case of $SnFe_2O_4$, this cubic spinel structure can be clearly identified through X-ray diffraction (XRD) analysis,[11] MCr_2S_4 (M = Fe & Co),[121] and Fe_3O_4.[122] For example, in the study conducted by Dey *et al.*,[121] using the compounds $FeCr_2S_4$ and $CoCr_2S_4$ with spinel structures synthesized through the solid-state reaction method, the XRD results in Fig. 5B, refined using Rietveld refinement, showed that the materials have a cubic FCC spinel structure (No. 277). The atomic positions in the unit cell were determined as 8a Fe (0, 0, 0), 16c Cr (0.625, 0.625, 0.625, 0.625), and 32e S ($x = y = z =$ 0.3841920 (4)) for $FeCr_2S_4$ and 8a Co (0, 0, 0), 16c Cr (0.625, 0.625, 0.625), and 32e S ($x = y = z = 0.3779778$ (4)) for $CoCr_2S_4$ (Fig. 5B(i)). The XRD plot also indicated that both materials have a single-phase without impurities. The lattice parameters for each material are $a = b = c = 9.9984$ (2) Å for $FeCr_2S_4$ and $a = b = c = 9.9263$ (2) Å for $CoCr_2S_4$ (Fig. 5B).

In the study conducted by Roy *et al.*, it was found that there is a significant difference in lattice parameters because of variations in material concentration. The crystal size of Fe_3O_4 material (Fig. 5C) with a concentration of 0.4 M was approximately 34 nm, whereas for a concentration of 0.05, the crystal size was approximately 23 nm.[122] Higher lattice strain occurs in materials with smaller crystal sizes, resulting from lower precursor concentrations. Small crystal sizes can lead to larger grain boundaries and higher defect concentrations. Defects can introduce imperfections in the crystal, causing intrinsic strain in the lattice.[114]

4.3.2 Morphological structure. In a study by Roy *et al.*, the synthesis of Fe_3O_4 material was carried out with varying concentrations of iron chloride, namely 0.4, 0.2, 0.1, and 0.05 M. The results in Fig. 5D show that the average particle size was the largest, reaching almost 50 nm, at a precursor concentration of 0.4 M. As the precursor concentration decreased to 0.05 M, the particle size reduced to nearly 21 nm. These data were then fitted by calculating the full-width at half maximum (FWHM) of the four samples, which were approximately 22, 20, 22, and 18 nm for concentrations of 0.4, 0.2, 0.1, and 0.05 M, respectively.[122] A higher full-width half maximum (FWHM) in the particle size distribution indicates a broader range of particle sizes. The crystallite size, morphology, and particle size of nanoparticles depend on several factors, including reaction temperature, solvent, surfactant, and precursor concentration.[123]

4.3.3 Magnetic properties. The magnetization curve of the spinel materials exhibits hysteresis characteristics that disappear when transitioning from 5 K to room temperature, and $SnFe_2O_4$ displays superparamagnetic magnetization (Fig. 5E). It's important to note that the non-linearity of the $M(H)$ curve indicates the onset of ferromagnetism in the system. When hysteresis loops are not form, it indicates coercivity below the blocking temperature (TB). The coercivity (H_c) increases with decreasing temperature and reaches a value of approximately H_c is in the range of 555.61 Oe at $T = 5$ K.[11] There are differences in the magnetization values that can be explained by size scaling,[124] In the Monte Carlo simulation method, the morphology of nanoparticles is considered perfect with a cubic shape, whereas in experiments, crystal defects are present in samples and may not be controlled.

Open Access Article. Published on 11 June 2024. Downloaded on 2/18/2026 10:19:39 AM. This article is licensed under a Creative Commons Attribution-NonCommercial 3.0 Unported Licence.

4.3.4 Electrical properties. The resistivity-temperature (ρ–T) curve of spinel material ($SnFe_2O_4$) indicates semiconductor behavior with a decrease in resistivity as the temperature increases. However, there was an increase in resistivity in the range of 250–280 K. This suggests that the application of a 5 T magnetic field significantly influences the electrical properties (resistivity) with respect temperature. The observed transitions in resistivity values occur over a wide range, influenced by the distribution of nanoparticle sizes and shapes, as well as the effects of both intra- and inter-particle magnetic interactions with respect to temperature.[125] Mounkachi *et al.* have demonstrated in a study that $SnFe_2O_4$ undergoes a change in behavior from metallic to semiconductor (Fig. 5F). This occurs when the distribution of Sn distribution changes from octahedral to tetrahedral.[126] The increase in resistivity at low temperatures, which commonly occurs, is considered a sign of resistance, such as tunneling insulation, within the system. The increase in resistivity with decreasing temperature may occur because of the weakening of double exchange (DE) interactions at irregular interfaces, resulting from damage to the Fe–O–Fe bonds on the nanoparticle surface and the breaking of lattice translational symmetry on the surface.[127]

4.3.5 Magnetoresistance (MR) properties. Magnetoresistance (MR) in granular systems is generally negative. Fig. 5G show that at low fields, below a few hundred Oersteds, the resistivity value rapidly decreases with an increase in the magnetic field. At low temperatures, tunneling between neighboring grains is hindered by the charge accumulated on the small grains. This effect is known as Coulomb blocking (CB). The non-linear resistivity effect at low temperatures is typically associated with tunneling resistance on the particle surface.[128] These results are moderate than other oxides,[129] and much higher than those for other metal oxides, such as $Zn_{0.80}Co_{0.20}$-Fe_2O_4 (%MR) about 20%,[130] $Zn_{1-x}Ni_xFe_2O_4$ (%MR) about 30%[131] $Ni_{1-x}Mn_xFe_2O$,[132] and some manganite oxides.[133]

4.4 Kagome magnet

Magnets with a Kagome lattice structure have long been studied in condensed matter physics. The Kagome lattice forms a two-dimensional honeycomb network of triangles at various angles. Because of its unique lattice geometry, Kagome magnets to exhibit diverse topological states and phenomena.[15] In the compound RMn_6Sn_6, if the R element can be entirely replaced by elements such as Li, Mg, or Ca, it will result in ferromagnetic properties. The lower the valence of Li, Mg, and Ca, the fewer valence electron systems there will be. Therefore, by controlling the magnetic and electronic states, it possible to achieve a larger anomalous Hall effect and observe other phenomena. To investigate these phenomena, the Kagome lattice with d-electrons needs to be studied, designed to enhance the large numbers massive Dirac fermions in the ferromagnetic state.[13] By incorporating spin–orbit coupling and magnetism, the system can exhibit various nontrivial electronic or magnetic topological states, such as magnetic Weyl fermions, quantized anomalous Hall states, and spin structures.[14]

In the rare-earth Kagome magnet family $ReMn_6Sn_6$ (where Re is a rare-earth element) with a layered hexagonal structure, rich magnetic states and a nontrivial band structure topology is observed (Fig. 6A).[134] These materials typically consist of two magnetic sublattices from different layers: (1) a Kagome magnetic sublattice by Mn ions, and (2) a Kagome magnetic sublattice by rare-earth ions. Interlayer magnetic interactions drive various magnetic structures and produce complex magnetic phase diagrams. One example of such a material is $TmMn_6Sn_6$. $TmMn_6Sn_6$ forms a hexagonal structure with space group $P6/mmm$, consisting of Mn_3Sn Kagome planes separated by two Sn_3 layers and two inequivalent Sn_2Tm layers. Than light rare-earth elements such as Y, Tm is a heavy rare-earth element with 4f electrons and strong spin–orbit coupling, leading to stronger magnetic interactions capable of producing more complex magnetic states.[16] The Kagome magnet with the formula RMn_6Sn_6 (R = lanthanide) has recently been extensively studied because of its significance in magnetic transport properties for exploring new magnetic ground states and topological phases. The quasi-two-dimensional magnetic structure leads to strong intralayer coupling and weak interlayer coupling, which is highly sensitive to the sublattice properties. Than non-rare-earth Kagome materials such as $MgMn_6Sn_6$ and $LiMn_6Sn_6$, rare-earth metal compositions RMn_6Sn_6 exhibit more complex and tunable magnetic properties. By varying the R site, the magnetic properties can change dramatically. When R = Y, Sc, and Lu, the RMn_6Sn_6 system shows antiferromagnetic (AFM) behavior, whereas when R = Gd–Ho, the materials exhibit ferrimagnetic (FIM) behavior. Among the rare-earth metal alloys RMn_6Sn_6, $TmMn_6Sn_6$ exhibits a more complex magnetic structure than other alloys because of its dual magnetic sublattices and non-collinear magnetic structure with a Néel temperature $T_N = 350$ K. The exchange coupling interaction between neighboring Tm and Mn is antiferromagnetic (AFM). This Kagome magnet shows a transition temperature above room temperature (T_C), but the resulting magnetoresistance (MR) values are in the range of 6% to −3% over the temperature range of 10 K to 300 K with an applied magnetic field parallel to the sample of 6 T.[25]

The following describes the crystal structure, magnetic properties, electrical properties, and MR of Kagome magnets.

4.4.1 Crystal structure. The crystal structure of $TmMn_6Sn_6$ can be schematically represented as shown in Fig. 6A(i) and (ii). Fig. 6A(iii) shows the diffraction pattern of the Kagome material $TmMn_6Sn_6$ with pure phase. The magnetic diffraction pattern, namely the Kagome lattice, in the material $TmMn_6Sn_6$ forms a hexagonal structure with atoms located in the ab plane, as depicted in Fig. 6(iv).[25] In research by Ya *et al.*, showed that the ferromagnetic Kagome magnet Fe_3Sn_2 has a structure similar to a that of hexagonal graphene lattice.[13]

4.4.2 Electrical properties & magnetic properties. Fig. 6B(i) shows the resistivity–temperature curve (ρ–T) of $TmMn_6Sn_6$ material with current flowing along the *ab*-axis. The curve indicates metallic behavior in the material. The magnetic properties of $TmMn_6Sn_6$ in Fig. 6B(ii) show that magnetization increases rapidly after a previous slow increase at $H \perp c$. This increase in magnetization is associated with a spin-flop transition, indicating a complex magnetic structure transition at $H \perp c$. Conversely, at $H \| c$, the magnetization shows a linear increase. This suggests a difference in magnetization behavior

© 2024 The Author(s). Published by the Royal Society of Chemistry

Open Access Article. Published on 11 June 2024. Downloaded on 2/18/2026 10:19:39 AM.
This article is licensed under a Creative Commons Attribution-NonCommercial 3.0 Unported Licence.

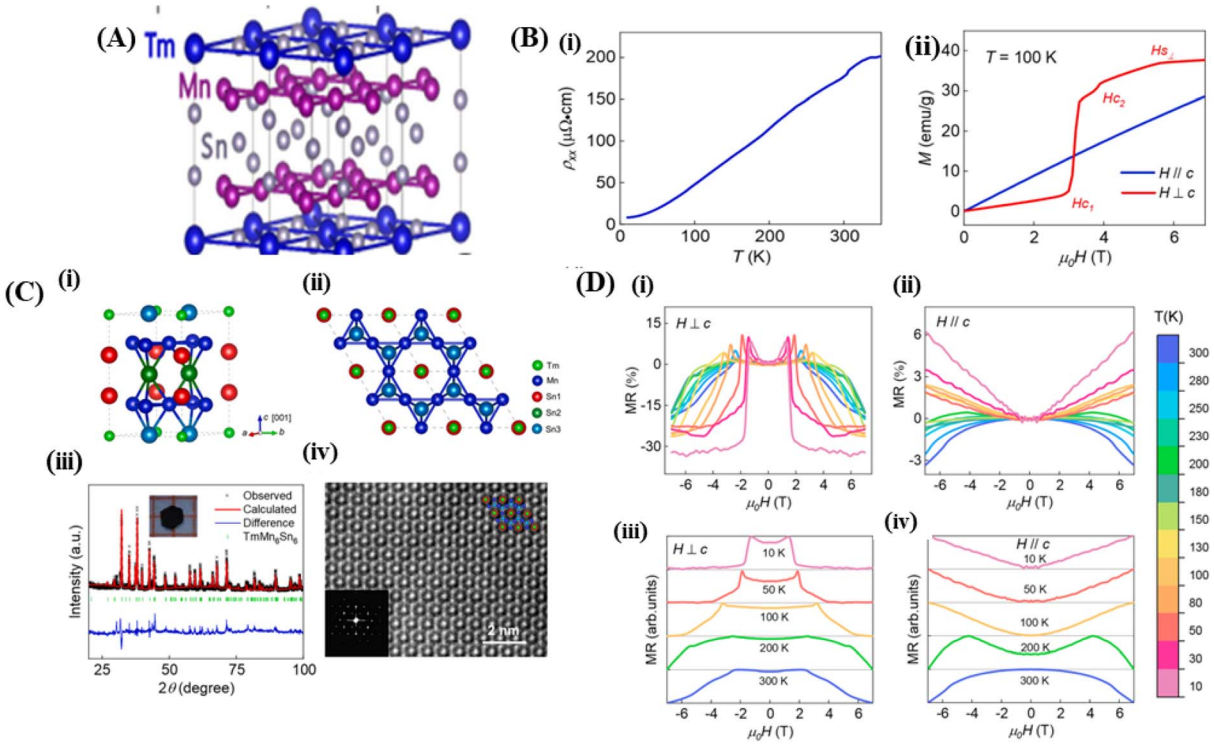

Fig. 6 [A] Crystal structure of Kagome ($TmMn_6Sn_6$). Reprinted with permission from the *Physical Review B*.[16] [B] (i) Crystal structure of $TmMn_6Sn_6$. (ii) The $TmMn_6Sn_6$ crystal structure is depicted in the illustration arranged along the [001] direction (iii) XRD pattern of $TmMn_6Sn_6$, (iv) l STEM image of $TmMn_6Sn_6$. Reprinted with permission from the Elsevier.[25] [C] (i) Resistivity *versus* temperature with current along the *ab*-axis. (ii) *M*(*H*) curves for $H||c$ and $H\perp c$ magnetic fields at 100 K. Reprinted with permission from the Elsevier.[25] [D] (i) and (ii) Magnetoresistance to field at various temperatures measured with $H\perp c$ and (ii) and (iv) $H||c$ Reprinted with permission from the Elsevier.[25]

between $H\perp c$ and $H||c$. The susceptibility of $TmMn_6Sn_6$ at $H\perp c$ is smaller than at $H||c$.

4.4.3 Magnetoresistance (MR) properties. The magnetoresistance (MR) of the Kagome lattice $TmMn_6Sn_6$ depends on temperature. MR increases and becomes more positive with increasing magnetic field when $H||c$. However, in the case of $H\perp c$, MR increases, but after reaching a maximum value at the critical magnetic field, MR rapidly decreases and become negative with increasing magnetic field, forming a saddle as shown in Fig. 6D(i) and (iii). Fig. 6D(iii) also shows significant changes that depend on temperature. However, the MR value when $H||c$ always remains positive at temperatures below 100 K and always negative at temperatures above 250 K (Fig. 6D(ii) and (iv)). For the MR curve with $H||c$, it shows a saddle-shaped curve where its value changes from positive to negative with increasing external magnetic field, but the indicated change is smaller. At $H||c$, it is positive when the temperature is above 250 K and always negative at temperatures below 100 K. At 150 K, the MR behavior was the same for both $H||c$ and $H\perp c$ (Tables 1–4).[25]

Based on the MR parameter data above, it can be concluded that there are several criteria for obtaining materials with high MR values, including the following:

1. Magnetic properties
(a) High saturation magnetization (M_s) value
(b) Low coercivity (H_c) value
(c) T_C near room temperature
2. Electrical properties
(a) Large resistivity change value
(b) T_ρ near room temperature
3. Low external magnetic field required (Table 5).

5. Electrical transport mechanism

To study the electron transport mechanism in materials, Nguyen *et al.* utilized a theoretical model to describe it. In the paramagnetic region, at high temperatures ($T > T_\rho$), the conductivity of manganites is generated through the thermally activated hopping of charge carriers localized in the form of small polaron. Therefore, the transport characteristics are described by two models: the variable-range hopping (VRH) model and the small polaron hopping (SPH) mechanism when $T < \theta_D/2$, where $\theta_D/2$ is the Debye temperature, which is the temperature at which the resistivity deviates from linearity in the plot $\ln(\rho/T)$ *versus* $1/T$. The conductivity mechanism in the range of $\theta_D/2 < T < T_\rho$ is analyzed using the VRH model, whereas for the range above $\theta_D/2$ it is described using the SPH model. In the SPH model, there are two different mechanisms, namely, adiabatic and non-adiabatic, as presented in the following equations:

$$\rho(T) = AT\exp\left(\frac{E_p}{k_B T}\right) \quad (5)$$

$$\rho(T) = AT^{3/2}\exp\left(\frac{E_p}{k_B T}\right) \quad (6)$$

Open Access Article. Published on 11 June 2024. Downloaded on 2/18/2026 10:19:39 AM.
This article is licensed under a Creative Commons Attribution-NonCommercial 3.0 Unported Licence.

Table 1 Magnetoresistance properties with parameters of magnetic properties, electrical properties, and MR of several perovskite materials

	Magnetic properties			Electrical properties		MR				
Sample	M_s (emu g^{-1})	H_c	T_c (K)	$\rho(H)$ (Ω cm)	T_ρ (K)	|MR| (%)	T_{MR} (K)	$(\mu_0 H)$ B	Method	Ref.
$La_{0.8}MnO_{3-\delta}$	45.71	—	268	0.2	260	90	260	5 T	Ceramic classical	149
$La_{0.85}MnO_3$	80	—	270	300	250	74	260	5 T	SS	150
$La_{0.7}Sr_{0.3}MnO_3$	50	—	>300	1.854	252	2	300	0.2 T	SG	22
$La_{0.7}Sr_{0.3}MnO_3$	—	—	>300	3.77×10^{-3}	>300	2	300	1 T	SS	22
$La_{0.875}Sr_{0.125}MnO_3$	—	—	—	0.029	290	32.22	273.22	1 T	SG-spin coating	151
$La_{0.850}Sr_{0.150}MnO_3$	—	—	—	0.012	300	42.85	290.95	1T	SG-spin coating	151
$La_{0.875}Sr_{0.175}MnO_3$	—	—	—	0.010	325	31.36	307.23	1T	SG-spin coating	151
$La_{0.800}Sr_{0.200}MnO_3$	—	—	—	0.008	350	25.76	315.64	1T	SG-spin coating	151
$La_{0.67}Sr_{0.33}MnO_3$	2.35	50	300	0.1	300	25	300	10 T	SS	56
$La_{0.8}Sr_{0.2}MnO_3$	—	—	—	0.01	300	27	200	0.5 T	SS	39
$La_{0.67}Sr_{0.33}MnO_3$	—	—	350	28	230	20	300	6 T	Citrate gel	152
$La_{0.67}Sr_{0.33}MnO_3$	32	—	>350	0.325	300	99	300	1 T	SG	153
$La_{0.67}Sr_{0.33}Mn_{0.95}Fe_{0.05}O_3$	15	—	350	1.6	225	97.5	300	1 T	SG	153
$La_{0.67}Sr_{0.33}Mn_{0.90}Fe_{0.10}O_3$	4	—	350	1000	—	100	300	1 T	SG	153
$La_{0.67}Sr_{0.33}Mn_{0.85}Fe_{0.15}O_3$	2	—	350	2500	—	100	300	1 T	SG	153
$La_{0.7}Ca_{0.3}MnO_3$	—	—	250	0.06	200	0.05	180	0.3 T	SS	40
$La_{0.75}Ca_{0.25}MnO_3$	—	—	350	40	270	80	250	4 T	—	154
$La_{0.72}Ca_{0.28}MnO_3$	—	—	—	0.015	290	57.1	260	1 T	SG	21
$La_{0.7}Ca_{0.3}MnO_3$	—	—	—	0.012	285	57.2	263	1T	SG	21
$La_{0.67}Ca_{0.33}MnO_3$	—	—	—	0.008	295	68.6	270	1T	SG	21
$La_{0.65}Ca_{0.35}MnO_3$	—	—	—	0.009	290	65.2	269	1T	SG	21
$La_{0.675}Ca_{0.375}MnO_3$	—	—	—	0.012	280	56	261	1 T	SG	21
$La_{0.65}Ca_{0.35}MnO_3$	—	—	—	0.29	225	57	260	8 T	SS	69
$La_{0.65}Ca_{0.30}Ba_{0.05}MnO_3$	—	—	—	0.37	140	55	260	8 T	SS	69
$La_{0.65}Ca_{0.25}Ba_{0.10}MnO_3$	—	—	—	0.51	225	45	280	8 T	SS	69
$La_{0.65}Ca_{0.20}Ba_{0.10}MnO_3$	—	—	—	0.15	270	43	290	8 T	SS	69
$La_{0.65}Ca_{0.15}Ba_{0.15}MnO_3$	—	—	—	0.09	180	32	300	8 T	SS	69
$La_{0.67}Ca_{0.33}MnO_3$	60	0.01 T	252.8	0.15	215.7	40.4	250	3 T	SS	7
$La_{0.67}Ca_{0.33}MnO_3$	—	—	—	0.0375	275	39.97	264.78	1 T	SS	155
$La_{0.67}Ca_{0.33}MnO_3$	—	—	—	0.022	275	54.27	263.80	1 T	SG	155
$La_{0.75}Ca_{0.25}MnO_3$	—	—	350	40	280	80	250	4 T	Mixing stoichiometric	156
$La_{0.7}Ca_{0.3}MnO_3$	—	—	—	0.2	260	18	77	3.6 T	SG	38
$La_{0.7}Ca_{0.3}MnO_3$	—	—	320	80	250	5	300	1 T	Citrate gel method	157
$La_{0.7}Ca_{0.3}MnO_3$	—	—	320	60	250	20	300	3 T	Citrate gel method	157
$La_{0.7}Ca_{0.3}MnO_3$	—	—	320	45	250	40	300	7 T	Citrate gel method	157
$La_{0.7}Ca_{0.3}MnO_3$	—	—	234	8	125	22	80	1 T	Pyrophoric reaction process	158
$La_{0.7}Ca_{0.3}MnO_3$	—	—	234	8	125	22	80	1 T	Pyrophoric reaction process	158
$La_{0.99}Na_{0.01}MnO_3$	—	—	210	0.175	240	75	240	1 T	SS	159
$La_{0.99}Na_{0.01}MnO_3$	—	—	—	0.10	260	60	240	3 T	SS	159
$La_{0.99}Na_{0.01}MnO_3$	—	—	—	0.075	290	50	240	5 T	SS	159
$La_{0.98}Na_{0.02}MnO_3$	—		225	0.10	250	70	250	1 T	SS	159
$La_{0.98}Na_{0.02}MnO_3$	—	—	—	0.06	270	55	250	3 T	SS	159
$La_{0.98}Na_{0.02}MnO_3$	—	—	—	0.05	300	30	250	5 T	SS	159
$La_{0.95}Na_{0.05}MnO_3$	—		240	0.075	260	70	260	1 T	SS	159

© 2024 The Author(s). Published by the Royal Society of Chemistry

Open Access Article. Published on 11 June 2024. Downloaded on 2/18/2026 10:19:39 AM.
This article is licensed under a Creative Commons Attribution-NonCommercial 3.0 Unported Licence.

Table 1 (*Contd.*)

Sample	Magnetic properties			Electrical properties		MR			Method	Ref.
	M_s (emu g^{-1})	H_c	T_c (K)	$\rho(H)$ (Ω cm)	T_ρ (K)	|MR| (%)	T_{MR} (K)	$(\mu_0 H)$ B		
$La_{0.95}Na_{0.05}MnO_3$	—	—	—	0.05	280	52	260	3 T	SS	159
$La_{0.95}Na_{0.05}MnO_3$	—	—	—	0.04	290	28	260	5 T	SS	159
$La_{0.8}Na_{0.2}MnO_3$	—	—	—	7.5×10^{-5}	350	15	320	2 T	SS	96
$La_{0.8}Na_{0.2}MnO_3$	—	—	—	8×10^{-5}	330	25	340	5 T	SS	96
$La_{0.8}Na_{0.15}\square_{0.05}MnO_3$	—	—	—	1.6×10^{-5}	340	22	320	2 T	SS	96
$La_{0.8}Na_{0.15}\square_{0.05}MnO_3$	—	—	—	2.0×10^{-5}	320	38	320	5 T	SS	96
$La_{0.8}Na_{0.1}\square_{0.1}MnO_3$	—	—	—	1.4×10^{-5}	310	35	300	2 T	SS	96
$La_{0.8}Na_{0.1}\square_{0.1}MnO_3$	—	—	—	1.9×10^{-5}	300	50	300	5 T	SS	96
$La_{0.8}\square_{0.15}MnO_3$	—	—	—	6.0×10^{-5}	300	40	280	2 T	SS	96
$La_{0.8}\square_{0.15}MnO_3$	—	—	—	9.0×10^{-5}	290	60	290	5 T	SS	96
$La_{0.9}K_{0.1}MnO_3$	—	—	—	0.030	300	43.03	286.3	1T	SG	160
$La_{0.85}K_{0.15}MnO_3$	—	—	—	0.028	>300	46.39	294.03	1T	SG	160
$La_{0.8}K_{0.2}MnO_3$	—	—	—	0.025	>300	37.49	294.6	1T	SG	160
$La_{0.75}K_{0.25}MnO_3$	—	—	—	0.020	>300	35.16	295.43	1T	SG	160
$La_{0.7}K_{0.3}MnO_3$	—	—	—	0.017	>300	26.76	296.4	1T	SG	160
$La_{0.833}K_{0.167}MnO_3$	90	—	277	2.5	250	0.4	320	5.5 T	SG	161
$La_{0.67}K_{0.33}MnO_3$	—	—	325	22	290	40	300	6 T	SG	58
$La_{0.95}K_{0.05}MnO_3$	—	—	260.45	0.339	239.8	0.40	300	0.8 T	Thermolysis of an aqueous	162
$La_{0.90}K_{0.10}MnO_3$	—	—	287.43	0.281	261.9	2.82	300	0.8 T	Thermolysis of an aqueous	162
$La_{0.85}K_{0.15}MnO_3$	—	—	309.76	0.189	276.0	4.53	300	0.8 T	Thermolysis of an aqueous	162
$LaMnO_{3+\delta}$	—	—	150	5.00	150	0.07	175	0.6 T	Precursor-based synthetic	163
$La_{0.95}$ $K_{0.05}MnO_{3+\delta}$	—	—	235	1.2	230	0.08	225	0.6 T	Precursor-based synthetic	163
$La_{0.85}K_{0.15}MnO_3$	44.34	31.252 G	360	0.1	289	6	300	1 T	SS	164
$La_{0.85}K_{0.15}MnO_3$	34.58	29.115 G	360	1.1	289	3.5	300	1 T	SG	164
$La_{0.85}K_{0.15}MnO_3$	23.56	10.986 G	320	11	258	8	300	1 T	Co-precipitation	164
$(La_{0.5}Pb_{0.5})MnO_3$	—	—	—	0.02	>300	18	300	5 T	SG	165
$(La_{0.6}Pb_{0.4})_{0.95}MnO_3$	—	—	—	0.022	>300	20	300	5 T	SG	165
$(La_{0.8}Pb_{0.2})_{0.9}MnO_3$	—	—	—	0.0325	>300	24	300	5 T	SG	165
$La_{0.5}Pb_{0.5}MnO_3$	—	—	—	1.26	225	2.5	300	1.5 T	SS	145
$La_{0.8}Ca_{0.2}MnO_3$	—	—	241	0.075	290	28	250	2 T	SS	97
$La_{0.8}Ca_{0.1}\square_{0.1}MnO_3$	—	—	264	0.03	240	27	260	2 T	SS	97
$La_{0.8}\square_{0.2}MnO_3$	—	—	259	0.225	240	10	270	2 T	SS	97
$La_{0.5}Nd_{0.15}Ca_{0.35}MnO_3$	75	—	204	0.3	200	63	208	4 T	*Via* ceramic	148
$La_{0.5}Nd_{0.15}Ca_{0.25}Li_{0.1}MnO_3$	80	—	169	10	160	72	171	4 T	*Via* ceramic	148
$La_{0.5}Nd_{0.15}Ca_{0.25}Na_{0.1}MnO_3$	90	—	263	20	180	57	184	4 T	*Via* ceramic	148
$La_{0.5}Nd_{0.15}Ca_{0.25}K_{0.1}MnO_3$	100	—	266	0.2	240	71	207	4 T	*Via* ceramic	148
$La_{0.7}Ba_{0.1}Ca_{0.1}Sr_{0.1}MnO_3$	95	—	330.81	0.012	250	32	275	7 T	SG	68
$La_{0.7}Ba_{0.1}Ca_{0.1}Sr_{0.1}MnO_3$	93	—	316.17	0.008	275	32.5	274	7 T	WM	68
$Nd_{0.7}Sr_{0.3}MnO_3$	5	—	255	1293	154	1	300	0.2 T	Chemical citrate-gel route	22
$Nd_{0.7}Sr_{0.3}MnO_3$	—	—	270	5.33×10^{-2}	252	2	300	0.2 T	Chemical citrate-gel route	22
$Nd_{0.67}Ca_{0.33}MnO_3$	—	—	—	9×10^3	120	20	250	7 T	SG	72
$Nd_{0.67}Sr_{0.33}MnO_3$	—	—	—	9	250	18	225	7 T	SG	72
$Nd_{0.67}Pb_{0.33}MnO_3$	—	—	—	15	175	80	150	7 T	SG	72
$Nd_{0.67}Ba_{0.33}MnO_3$	—	—	—	500	150	90	90	7 T	SG	72

© 2024 The Author(s). Published by the Royal Society of Chemistry

Open Access Article. Published on 11 June 2024. Downloaded on 2/18/2026 10:19:39 AM.
This article is licensed under a Creative Commons Attribution-NonCommercial 3.0 Unported Licence.

Table 1 (*Contd.*)

Sample	Magnetic properties			Electrical properties		MR			Method	Ref.
	M_s (emu g^{-1})	H_c	T_c (K)	$\rho(H)$ (Ω cm)	T_ρ (K)	|MR| (%)	T_{MR} (K)	($\mu_0 H$) B		
$(Pr_{1/3}Sm_{2/3})_{2/3}Sr_{1/3}MnO_3$	3.5	—	150	4	156	95	150	8 T	Chemical citrate-gel route	138
$(Pr_{1/3}Sm_{2/3})_{2/3}Sr_{1/3}MnO_3$	3.5	—	150	6	156	90	150	6 T	Chemical citrate-gel route	138
$(Pr_{1/3}Sm_{2/3})_{2/3}Sr_{1/3}MnO_3$	3.5	—	150	7	156	82	150	4 T	Chemical citrate-gel route	138
$(Pr_{1/3}Sm_{2/3})_{2/3}Sr_{1/3}MnO_3$	3.5	—	150	8	156	64	150	2 T	Chemical citrate-gel route	138
$(Pr_{1/3}Sm_{2/3})_{2/3}Ba_{1/3}MnO_3$	2.5	—	200	12	150	100	50	8 T	Chemical citrate-gel route	138
$(La_{1/3}Sm_{2/3})_{0.67}Ba_{0.33}MnO_3$	3.2	—	175	5×10^5	70	100	100	8 T	Chemical citrate-gel route	166
$(La_{1/3}Sm_{2/3})_{0.67}Ba_{0.23}Sr_{0.1}MnO_3$	3.5	—	175	10^4	75	90	100	8 T	Chemical citrate-gel route	166
$(La_{1/3}Sm_{2/3})_{0.67}Ba_{0.13}Sr_{0.2}MnO_3$	3.5	—	175	10^3	100	100	110	8 T	Chemical citrate-gel route	166
$(La_{1/3}Sm_{2/3})_{0.67}Sr_{0.33}MnO_3$	3.4	—	175	10	200	80	200	8 T	Chemical citrate-gel route	166
$La_{0.833}Li_{0.167}MnO_3$	70.1	145	113	0.1	75	86.8	75	5 T	SG	59
$La_{0.85}K_{0.15}MnO_3$	23.56	10.986 G	320	11	258	8	300	1 T	Co-precipitation	164
$(La_{0.5}Pb_{0.5})MnO_3$	—	—	—	0.02	>300	18	300	5 T	SG	165
$La_{0.7}Ca_{0.3}MnO_3$	—	—	234	8	125	22	80	1 T	Pyrophoric reaction process	158
$La_{0.99}Na_{0.01}MnO_3$	—	—	210	0.175	240	75	240	1 T	SS	159
$La_{0.99}Na_{0.01}MnO_3$	—	—	—	0.10	260	60	240	3 T	SS	159
$La_{0.99}Na_{0.01}MnO_3$	—	—	—	0.075	290	50	240	5 T	SS	159
$La_{0.98}Na_{0.02}MnO_3$	—		225	0.10	250	70	250	1 T	SS	159
$La_{0.98}Na_{0.02}MnO_3$	—	—	—	0.06	270	55	250	3 T	SS	159
$La_{0.98}Na_{0.02}MnO_3$	—	—	—	0.05	300	30	250	5 T	SS	159
$La_{0.95}Na_{0.05}MnO_3$	—		240	0.075	260	70	260	1 T	SS	159
$La_{0.95}Na_{0.05}MnO_3$	—	—	—	0.05	280	52	260	3 T	SS	159
$La_{0.95}Na_{0.05}MnO_3$	—	—	—	0.04	290	28	260	5 T	SS	159
$La_{0.8}Na_{0.2}MnO_3$	—	—	—	7.5×10^{-5}	350	15	320	2 T	SS	96
$La_{0.8}Na_{0.2}MnO_3$	—	—	—	8×10^{-5}	330	25	340	5 T	SS	96
$La_{0.833}Na_{0.167}MnO_3$	84.2	66	308	1.6	309	33.7	309	5 T	SG	59
$La_{0.833}Ag_{0.167}MnO_3$	75.2	40	296	0.8	299	37.4	299	5 T	SG	59
$La_{0.833}K_{0.167}MnO_3$	76.7	83	320	1.6	328	27.2	328	5 T	SG	59
$La_{0.80}Sm_{0.05}Na_{0.15}MnO_3$	—	—	—	2.25	280	10	250	8 T	SS	167
$La_{0.80}Sm_{0.05}Na_{0.15}MnO_3$	—	—	—	1.6	290	18	250	4 T	SS	167
$La_{0.80}Sm_{0.05}Na_{0.15}MnO_3$	—	—	—	0.8	300	9	250	2 T	SS	167
$La_{0.75}Sm_{0.1}Na_{0.15}MnO_3$	—	—	—	0.8	250	40	250	8 T	SS	167
$La_{0.75}Sm_{0.1}Na_{0.15}MnO_3$	—	—	—	0.7	250	25	250	4 T	SS	167
$La_{0.75}Sm_{0.1}Na_{0.15}MnO_3$	—	—	—	0.6	250	12	250	2 T	SS	167
$La_{0.70}Sm_{0.15}Na_{0.15}MnO_3$	—	—	—	0.9	250	64	250	8 T	SS	167
$La_{0.70}Sm_{0.15}Na_{0.15}MnO_3$	—	—	—	0.8	250	52	250	4 T	SS	167
$La_{0.70}Sm_{0.15}Na_{0.15}MnO_3$	—	—	—	0.6	250	40	250	2 T	SS	167
$Y_{0.15}Ca_{0.85}MnO_3$	1.5	—	150	0.12	80	50	100	5 T	SS	168
$Y_{0.15}Ca_{0.85}MnO_3$	1.5	—	150	0.07	90	60	100	7 T	SS	168
$Gd_{0.15}Ca_{0.85}MnO_3$	3	—	180	0.0065	90	50	100	5 T	SS	168
$Gd_{0.15}Ca_{0.85}MnO_3$	3	—	180	0.0045	110	60	100	7 T	SS	168
$Dy_{0.15}Ca_{0.85}MnO_3$	2.5	—	140	0.0075	100	50	100	5 T	SS	168
$Dy_{0.15}Ca_{0.85}MnO_3$	2.5	—	140	0.0065	100	60	100	7 T	SS	168
$(La_{0.7}Ca_{0.3}MnO_3)$	—	—	—	100	225	0.7	225	5 T	SG	43
$(La_{0.7}Ca_{0.3}MnO_3)_{0.95}$:$_{0.05}ZrO_2$	—	—	—	225	120	0.9	140	5 T	SG	43

© 2024 The Author(s). Published by the Royal Society of Chemistry

Open Access Article. Published on 11 June 2024. Downloaded on 2/18/2026 10:19:39 AM.
This article is licensed under a Creative Commons Attribution-NonCommercial 3.0 Unported Licence.

Table 1 (*Contd.*)

Sample	Magnetic properties			Electrical properties		MR			Method	Ref.
	M_s (emu g^{-1})	H_c	T_c (K)	$\rho(H)$ (Ω cm)	T_ρ (K)	|MR| (%)	T_{MR} (K)	$(\mu_0 H)$ B		
$(La_{0.7}Ca_{0.3}MnO_3)_{0.9}$:$_{0.1}ZrO_2$	—	—	—	120	120	0.8	160	5 T	SG	43
$(La_{0.7}Ca_{0.3}MnO_3)_{0.8}$:$_{0.2}ZrO_2$	—	—	—	225	160	0.8	140	5 T	SG	43
$(La_{0.7}Ca_{0.3}MnO_3)_{0.6}$:$_{0.4}ZrO_2$	—	—	—	40	200	0.8	200	5 T	SG	43
$La_{0.8}Ag_{0.2}MnO_3$	—	—	285	3.714×10^{-6}	289	5	220	0.7 T	SS	90
$_{(0.985)}La_{0.8}Ag_{0.2}MnO_3/_{0.015}BFO$	—	—	283	1.294×10^{-6}	282	8	230	0.7 T	SS	90
$_{(0.975)}La_{0.8}Ag_{0.2}MnO_3/_{0.025}BFO$	—	—	282	3.519×10^{-6}	278	6	240	0.7 T	SS	90
$_{(0.965)}La_{0.8}Ag_{0.2}MnO_3/_{0.035}BFO$	—	—	274	10.53×10^{-6}	272	18	280	0.7 T	SS	90
$La_{0.7}Sr_{0.3}MnO_3$	63		360	2.5×10^{4}	275	0.25	300	3 T	SS	94

In the study by Das *et al.*,[135] resistivity data were also analyzed using the small-polaron hopping model with different models, as follows:

$$\rho_{hop} = \frac{AT}{n}\left[1 + \left\{1 - c' m^2(t)\right\}\sigma_a{}^2\right]\cosh^2\left(\frac{\varepsilon_p}{2(T+\theta)}\right)\exp\left(\frac{U}{T}\right) \quad (7)$$

where $A = 1.13k_B/\nu_{ph}a^2e^2$, ν_{ph} is the frequency of the longitudinal optical phonon mode to which the electron with charge e is coupled, a is the distance of hopping, n is the density of charge carriers, σ_a is the short-range order parameter, ε_p is the small polaron stabilization energy and U is the activation energy of the charge carriers.[135]

Eqn (5) represents adiabatic small polaron hopping, and eqn (6) represents non-adiabatic small polaron hopping, where A is the residual resistivity, E_p is the activation energy of the polaron, is the band gap the polaron must overcome to transfer to the next site, which includes the activation energy required for free charge carriers (W_D) and the energy that stimulates carriers to hop (W_H), kB is the Boltzmann constant.

$$E_p = W_H + \frac{W_D}{2} \text{ for } T > \theta_D/2 \quad (8)$$

$$W_H = E_p - E_s \quad (9)$$

where W_H is polaron hopping energy, E_p is polaron activation energy, and E_s is thermoelectric activation energy.

In this case, the Holstein criterion can determine whether the polaron-hopping conduction is adiabatic or non-adiabatic. The Holstein criterion states that adiabatic and non-adiabatic mechanisms can be identified by comparing the polaron bandwidth (J) with the critical polaron energy bandwidth (ϕ), where the values of J and ϕ are determined from the following equations:

$$J(T) = 0.67h\nu_{ph}\left(\frac{T}{\theta_D}\right)^{1/4} \quad (10)$$

$$\phi(T) = \left(\frac{2k_B T W_H}{\pi}\right)^{1/4}\left(\frac{h\nu_{ph}}{\pi}\right)^{1/2} \quad (11)$$

where ν_{ph} is longitudinal optical phonon frequency, $h\nu_{ph} = k_B\theta_D$. If $J > \phi$, the conduction process is adiabatic small polaron hopping (ASPH), and if $J < \phi$, the conduction process is non-adiabatic small polaron hopping (NASPH).[136]

The temperature-dependent resistivity relationship can also be explained using the variable range hopping (VRH) model for the temperature range $T_\rho < T < \theta_D$, which is described by the following equation:

$$\sigma = \sigma_0 \exp\left(-\frac{T_0}{T}\right)^{1/4} \quad (12)$$

where $T_0 = 18/k_B N(E_F)\alpha^3$ is the Mott characteristic temperature, with α as the inverse of the localization length equal to 2.22 nm^{-1}, $N(E_F)$ is the density of states at the Fermi level[137]

Furthermore, in the study by Asthana *et al.*,[138] it was mentioned that the transport data in the semiconducting

Open Access Article. Published on 11 June 2024. Downloaded on 2/18/2026 10:19:39 AM. This article is licensed under a Creative Commons Attribution-NonCommercial 3.0 Unported Licence.

Table 2 Magnetoresistance properties with parameters of magnetic properties, electrical properties, and MR of some alloy materials

	Magnetic properties			Electrical properties		MR				
Sample	M_s (emu g^{-1})	Hc	T_C (K)	$\rho(H)$ (Ω cm)	T_ρ (K)	|MR| (%)	T_{MR} (K)	(μ_0H) B	Method	Ref.
$(Co_{0.79}Mn_{0.21})_{0.92}Fe_{0.08}$	1550	—	—	—	—	200	350	—	Arc melting	50
$(Co_{0.79}Mn_{0.21})_{0.83}Fe_{0.17}$	1550	—	—	—	—	290	370	—	Arc melting	50
$(Co_{0.79}Mn_{0.21})_{0.74}Fe_{0.26}$	1450	—	—	—	—	280	400	—	Arc melting	50
$(Co_{0.79}Mn_{0.21})_{0.65}Fe_{0.35}$	1400	—	—	—	—	220	430	—	Arc melting	50
$(Co_{0.79}Mn_{0.21})_{0.55}Fe_{0.45}$	1600	—	—	—	—	200	440	—	Arc melting	50
$Ni_{34}(FeCo)_{16}Mn_{37}Ti_{13}$	40	—	330	1.3	280	25.4	317	5 T	Arc melting	98
$Ni_{32}(FeCo)_{18}Mn_{37}Ti_{13}$	58	—	346	1.3	275	12.9	317	5 T	Arc melting	98
$Ni_{30}(FeCo)_{20}Mn_{37}Ti_{13}$	65	—	369	1.4	200	23.7	248	5 T	Arc melting	98
$Ni_{92}Cu_8$	0.8	—	—	—	—	1.4	—	1 T	Electrochemical deposition	99
$Ni_{75}Cu_{25}$	1.0	—	—	—	—	10	—	1 T	Electrochemical deposition	99
$Ni_{54}Cu_{46}$	0.9	—	—	—	—	0.8	—	1 T	Electrochemical deposition	99
$Ni_{46.8}Mn_{38.1}Sn_{11.6}Fe_{3.5}$	—	—	—	13	268	47	262	5 T	Induction melting	102
$Ni_{46.8}Mn_{38.1}Sn_{11.6}Fe_{3.5}$	—	—	—	14	276	25	262	2 T	Induction melting	102
$Ni_2Mn_{1.4}Sn_{0.6}$	60	—	—	200	160	16	170	5 T	Argon arc melting	120
$Ni_{45}Co_5Mn_{36.5}In_{13.5}$	—	—	300	0.8	200	80	230	5 T	Arc melting	114
$Ni_{40}Co_6Fe_4Mn_{33}Al_{17}$	211	—	348	0.06	250	35	230	3 T	Melting high purity	117
$Ni_{40}Co_4Fe_6Mn_{33}Al_{17}$	173	—	297	0.015	220	28	190	3 T	Melting high purity	117
$Ni_{40}Co_2Fe_8Mn_{33}Al_{17}$	127	—	—	0.005	170	15	150	3 T	Melting high purity	117
$Ni_{43}Mn_{41}Co_5Sn_{11}$	—	—	—	—	—	20	280	1 T	Arc melting high purity	118
$Mn_{1.9}Co_{0.1}Sb$	40	—	—	—	170	46	136	5 T	Arc melting	104
$Ni_{45}Mn_{43}CrSn_{11}$	50	—	300	28	250	70	250	5 T	Arc melting	105
$Ni_{50}Mn_{37}Sn_{13}$	—	—	300	108	320	24	320	5 T	Arc melting	169
$Ni_{50}Mn_{36}Sn_{14}$	—	—	220	120	250	42	250	5 T	Arc melting	169
$Ni_{50}Mn_{35}Sn_{15}$	—	—	180	90	180	42	180	5 T	Arc melting	169
$Ni_{50}Mn_{36}Sn_{16}$	—	—	100	40	100	34	100	5 T	Arc melting	169

regime of the material can be analyzed using Mott variable range hopping (Mott-VRH) with the following equation:

$$\rho = \rho_{0m} \exp(T_{0m}/T)^{1/4} \quad (13)$$

where ρ_{0m} is the Mott residual resistivity and T_{0m} is the Mott characteristic temperature.[138]

On the other hand, in the metallic region ($T_0 \leq T_\rho$), the electron transport mechanism is described by one of the following equations:

$$\rho(T) = \rho_0 + \rho_{2.5}T^{2.5} \quad (14)$$

$$\rho(T) = \rho_0 + \rho_2T^2 + \rho_{4.5}T^{4.5} \quad (15)$$

$$\rho(T) = \rho_0 + \rho_2T^2 + \rho_5T^5 \quad (16)$$

where ρ_0 is the resistivity because of grain/domain boundary effects, ρ_2T^2 represents the electrical resistivity because of the electron–electron scattering process, $\rho_{2.5}T^{2.5}$ is the electrical resistivity because of electron–magnon scattering process in the ferromagnetic phase, $\rho_{4.5}T^{4.5}$ is a combination of electron–electron, electron-magnon and electron–phonon scattering processes, and ρ_5T^5 term is accredited to the electron–phonon interaction.[96]

In the research of Khlifi *et al.*, it was shown that in the paramagnetic region, at high temperatures ($T > T_\rho$), the electrical conduction mechanism in the magnetic material ($La_{0.8}Ca_{0.2-x}\square_xMnO_3$) is governed by the adiabatic mechanism of small polaron hopping (SPH),[139] where

$$\rho_{PM}(T) = \rho_\alpha T \exp\left(\frac{E_a}{k_BT}\right) \quad (17)$$

where $\rho_\alpha = 2\ k_B/(3ne^2a^2v)$. The resistivity coefficient ρ_α is temperature-independent, where n is the charge carrier concentration, e is the electron charge, a represents the hopping distance, v is the frequency of longitudinal optical phonons, and E_a and kB respectively, represent the activation energy and the Boltzmann constant.[97]

At low temperatures ($T < T_\rho$), Khlifi *et al.*, used $\rho_{FM}(T)$ from eqn (15). The fitting results can be seen in Fig. 7 (A), showing a simulation of the resistivity *vs.* temperature curve using the formulas $\rho_{PM}(T)$ in the insulating phase (red line) and ρ_{FM} (T) (green line).

From the curve, it can be observed that the minimum resistivity is obtained at a temperature of 40 K. The scattering mechanism cannot explain the resistivity at lower temperature ranges (<40 K). This indicates that the contribution of other behaviors influences the resistivity at low temperatures. Essentially, this behavior is caused by strong correlation effects, related to the disordered system.[140] The origin of this low-temperature behavior is analyzed by considering scattering mechanisms such as the Kondo effect and electron–electron interactions.[141] To explain these mechanisms, experimental measurements are fitted with equations:

© 2024 The Author(s). Published by the Royal Society of Chemistry

Open Access Article. Published on 11 June 2024. Downloaded on 2/18/2026 10:19:39 AM. This article is licensed under a Creative Commons Attribution-NonCommercial 3.0 Unported Licence.

Table 3 Magnetoresistance properties with parameters of magnetic properties, electrical properties, and MR of some spinel materials[a]

	Magnetic properties			Electrical properties		MR				
Sample	M_s (emu g^{-1})	H_c	T_C (K)	$\rho(H)$ (Ω cm)	T_ρ (K)	$\lvert MR\rvert$ (%)	T_{MR} (K)	$(\mu_0 H)$ B	Method	Ref.
$FeCr_2Te_4$	—	—	—	1.1	>300	3.2	140	9 T	SS	12
$FeCr_2Te_4$	—	—	—	1.1	>300	2.4	140	7 T	SS	12
$FeCr_2Te_4$	2.2	—	123	1.1	>300	1.4	140	5 T	SS	12
$FeCr_2S_4$	24	50 kOe	170	48	175	17	165	50 kOe	SS	121
$CoCr_2S_4$	27	50 kOe	225	7×10^7	150	10.2	165	50 kOe	SS	121
$ZnFe_2O_4$	10	—	—	11	150	9	200	9 T	SS	130
$Zn_{0.8}Co_{0.2}Fe_2O_4$	50	0.3 T	170	36	150	12	200	9 T	SS	130
$Zn_{0.6}Co_{0.4}Fe_2O_4$	120	0.2 T	>300	43	150	16	200	9 T	SS	130
$ZnFe_2O_4$	—	—	—	—	—	4	250	9 T	SS	131
$Zn_{0.9}Ni_{0.1}Fe_2O_4$	30	005 T	—	—	—	6.25	250	9 T	SS	131
$Zn_{0.8}Ni_{0.2}Fe_2O_4$	60	0.05 T	150	—	—	5	250	9 T	SS	131
$Zn_{0.7}Ni_{0.3}Fe_2O_4$	100	0.05 T	—	—	—	7	250	9 T	SS	131
$Zn_{0.6}Ni_{0.4}Fe_2O_4$	140	0,05 T		—	—	9	250	9 T	SS	131
$Ni_{0.6}Mn_{0.4}Fe_2O_4$	51.76		229	—	—	0.43	502	0.57 T	SS	132
$Ni_{0.2}Mn_{0.8}Fe_2O_4$	58.13		210	—	—	1,24	438	057 T	SS	132
$SnFe_2O_4$	14.17	36,11 Oe	760	7×10^5	280	80.10	260	5 T	Solvo-thermal	11
Fe_3O_4	87.5	100 Oe	—	—	—	2.13	>300	5 kOe	Co-precipitation	122
$FeCr_{1.95}Ga_{0.05}S_4$	—	—	180	90	—	0.5	250	0.5 T	SS	173
$FeCr_{1.9}Ga_{0.1}S_4$	—	—	180	15	—	0.32	250	0.5 T	SS	173
$FeCr_{1.85}Ga_{0.15}S_4$	—	—	180	8	—	0.25	250	0.5 T	SS	173
$FeCr_{1.8}Ga_{0.2}S_4$	—	—	180	5	—	0.2	250	0.5 T	SS	173
$FeCr_{1.7}Ga_{0.3}S_4$	—	—	200	3	—	0.22	250	0.5 T	SS	173
$FeCr_{1.6}Ga_{0.4}S_4$	—	—	200	8	—	0.32	250	0.5 T	SS	173
$CdCr_2S_4$	6	—	85	120	125	55	90	9 T	Chemical transport reaction	174
$Fe_{2.5}Zn_5O_4$	12	—	—	—	—	30	300	1.2 T	Pulsed laser deposition	175
$Fe_{2.5}Mn_5O_4$	50	—	—	—	—	90	300	1.2 T	Pulsed laser deposition	175

[a] SG (sol–gel), SS (solid-state reaction), wet-mixing (WM).

$$\rho(T) = \frac{1}{\sigma(0) + BT^{\frac{1}{2}}} + AT^n \tag{18}$$

$$\rho(T) = \frac{1}{\sigma(0) + B\,\mathrm{Ln}\,T} + AT^n \tag{19}$$

Eqn (18) depends on electron–electron interactions, and eqn (19) depends on the influence of scattering like the Kondo effect. Here, r (0) represents the residual conductivity, the term $BT^{1/2}$ corresponds to correlated electron–electron interactions, and the term B Ln (T) represents the contribution because of the spin dependence of scattering, like the Kondo effect. Eqn (18) is used for samples with a 0 T field effect, whereas eqn (19) is used for samples under 2 and 5 T fields. Fig. 7B shows a good fit between the equation results and experimental data. This concludes that the mechanism responsible for the increase in resistivity at low temperatures is sensitive to the applied magnetic field, regulated by Kondo-like scattering, which is consistent with the results obtained by Xu *et al.* in the compounds $La_{2/3}Ca_{1/3}MnO_3$ and electron–electron interactions.[142]

Meanwhereas, percolation approach is used for the electrical transport mechanism in the temperature range of 5–400 K, assuming that the material is composed of paramagnetic (PM) and ferromagnetic (FM) regions. In this approach, the electrical resistivity of the system is determined by the variation in the volume fraction of ferromagnetic regions (f). Thus, the resistivity is expressed by the equation:

$$\rho(T) = \rho_{FM} f + \rho_{PM}(1 - f) \tag{20}$$

where f and $(1 - f)$ are the volume fractions of the FM and PM states, respectively. The function f is determined through a mathematical combination as follows:

$$f = \frac{1}{1 + \exp\left(\frac{\Delta U}{k_B T}\right)},\ 1 - f = \frac{\exp\left(\frac{\Delta U}{k_B T}\right)}{1 + \exp\left(\frac{\Delta U}{k_B T}\right)},\ \Delta U = -U0\left(1 - \frac{1}{T_C^{\mathrm{mod}}}\right) \tag{21}$$

Then the equation $\rho(T)$ becomes:

Open Access Article. Published on 11 June 2024. Downloaded on 2/18/2026 10:19:39 AM. This article is licensed under a Creative Commons Attribution-NonCommercial 3.0 Unported Licence.

Table 4 Magnetoresistance properties with parameters of magnetic properties, electrical properties, and MR of some Kagome materials

	Magnetic properties			Electrical properties		MR				
Sample	M_s (emu g^{-1})	H_c	T_C (K)	$\rho(H)$ (Ω cm)	T_ρ (K)	|MR| (%)	T_{MR} (K)	$(\mu_0 H)$ B	Method	Ref.
CoSn	—	—	5	—	—	105	3	8 T	Arc melting	176
$Co_{0.8}Fe_{0.2}Sn$	—	—	17	—	—	8.4	3	8 T	Arc melting	176
$Co_{0.7}Fe_{0.3}Sn$	—	—	26	—	—	3.7	3	8 T	Arc melting	176
$Co_{0.6}Fe_{0.4}Sn$	—	—	—	—	—	2.7	3	8 T	Arc melting	176
$Co_3In_2S_2$	—	—	—	20	50	0.3	20	8 T	Flux method	177
$(Co_{0.97}Fe_{0.03})_3In_2S_2$	—	—	—	44	50	0.175	50	8 T	Flux method	177
Fe_3Sn_2	2.0 μ_B/Fe	—	320	250	400	2	40	9 T	Self-flux	178
YMn_6Sn_6	1.5 μ_B/Fe	—	400	0.08	400	24	40	9 T	Sn flux methods	179
$YMn_6Sn_{5.93}Ga_{0.07}$	2 μ_B/Fe	—	400	0.06	400	14	40	9 T	Sn flux methods	179
$YMn_6Sn_{5.87}Ga_{0.13}$	2 μ_B/Fe	—	400	0.058	400	7.5	40	9 T	Sn flux methods	179
$YMn_6Sn_{5.78}Ga_{0.22}$	2 μ_B/Fe	—	400	0.05	400	21	40	9 T	Sn flux methods	179
$YMn_6Sn_{5.70}Ga_{0.30}$	2 μ_B/Fe	—	400	0.045	400	7	40	9 T	Sn flux methods	179
$YMn_6Sn_{5.39}Ga_{0.61}$	2 μ_B/Fe	—	400	0.045	400	7.5	40	9 T	Sn flux methods	179
$Ni_3In_2S_2$	—	—	—	0.4	300	16	2	10 T	SS	180
$Yb_{0.5}Co_3Ge_3$	—	—	—	15	300	12.5	3	10 T	Sn flux	181

Table 5 Comparison of measurement parameters of perovskite, alloy, spinel, and Kagome material structures based on criteria for obtaining materials with high MR values above[a]

	Magnetic properties			Electrical properties		
Material group	*a*	*b*	*c*	*a*	*b*	Low $(\mu_0 H)$ B external
Perovskite	✓	✓	✓	✓	✓	✓
Alloy	✓	—	✓	—	✓	✓
Spinel	✓	✓	—	—	—	—
Kagome	—	—	✓	✓	✓	—

[a] ✓ = meets the criteria, — = not meeting the criteria.

$$\rho(T) = \rho_0 + \rho_2 T^2 + \rho_5 T^5 . \frac{1}{1+e^{\left(\frac{-U0\left(1-\frac{T}{T_C^{mod}}\right)}{k_B T}\right)}} + \rho_\alpha T \exp\frac{E_a}{k_B T} \frac{e^{\left(\frac{-U0\left(1-\frac{T}{T_C^{mod}}\right)}{k_B T}\right)}}{1+e^{\left(\frac{-U0\left(1-\frac{T}{T_C^{mod}}\right)}{k_B T}\right)}} \quad (22)$$

From Fig. 7C, it can be explained that $f(T)$ eqn (22) below the metal–insulator transition temperature, with a strong dominance of the FM fraction. Then, the volume fraction of FM reduces to zero, transitioning from the ferromagnetic metal state to the paramagnetic insulator state. The temperature-dependent variation of f confirms that it follows a Boltzmann distribution, being one below the transition temperature and 0 above the transition temperature.

Thus, the temperature-dependent resistivity variation for all temperature ranges can be expressed using the following equation:

$$\rho(T) = (1-f) \times \rho_\alpha T \exp\left(\frac{E_a}{k_B T}\right) + f \times \left(\rho_0 + \rho_2 T^2 + \rho_5 T^5\right) \quad (23)$$

Fig. 7D shows that the experimental results are in accordance with the equation, even with the influence of external magnetic fields of 0 T, 2 T, and 5 T. This result aligns with the research of Gamzatov *et al.*[143]

In the GMR effect, there are several mechanisms to consider related to the transition between antiferromagnetic (AF) and ferromagnetic (F) states. One mechanism is spin-dependent scattering of conduction electrons, associated with a decrease in relaxation time in the AF state. This mechanism generally leads to GMR in magnetic multilayers. GMR depends on both spin and electron conduction. GMR mechanisms not only assume that electron scattering occurs because of irregularities at layer boundaries; another possible GMR mechanism involves variations in the Fermi surface through metamagnetic transitions, resulting from the formation of superzone gaps in the AF state. To explain the origin of GMR mechanisms, measurements of transport properties such as the Hall effect and thermoelectric power are required. Hall resistivity in magnetic materials is divided into two types: normal Hall resistivity and extraordinary Hall resistivity. Normal Hall resistivity provides information about the Fermi surface, such as carrier concentration and the *k*-dependence of conduction electron scattering. The extraordinary Hall effect provides information about the asymmetry of scattering. Meanwhereas, thermoelectric power is a derivative of the energy density of states and the relaxation

© 2024 The Author(s). Published by the Royal Society of Chemistry

Open Access Article. Published on 11 June 2024. Downloaded on 2/18/2026 10:19:39 AM.
This article is licensed under a Creative Commons Attribution-NonCommercial 3.0 Unported Licence.

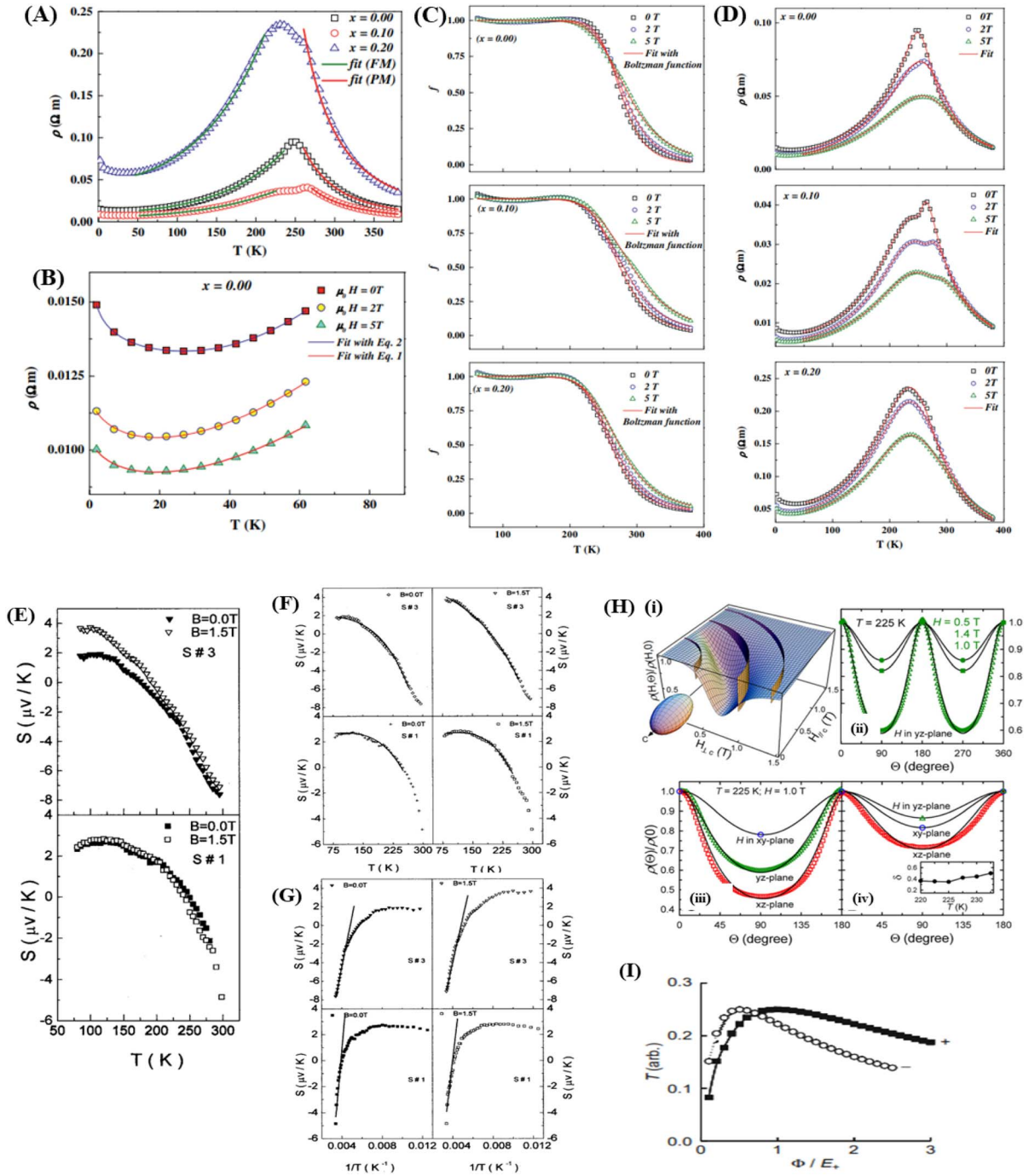

Fig. 7 [A] Resistivity variation as a function of temperature in the zero plane (symbol) for samples $x = 0.00$, $x = 0.10$ and $x = 0.20$, and resistivity fit Reprinted with permission from the Elsevier.[97] [B] Resistivity fit according to eqn (7) for $x = 0.00$, $x = 0.10$ and $x = 0.20$ samples in the temperature range between 0 and 100 K. Reprinted with permission from the Elsevier.[97] [C] Volume fraction of ferromagnetic phase (f) against temperature for different samples: $x = 0.00$, $x = 0.10$ and $x = 0.20$ under applied magnetic field of 0; 2 and 5 T) Reprinted with permission from the Elsevier.[97] [D] Experimental (symbols) and calculated (lines) electrical resistivity as a function of temperature of $x = 0.00$, $x = 0.10$ and $x = 0.20$ samples under the application of 0; 2 and 5 T magnetic field). Reprinted with permission from the Elsevier.[97] [E] The thermal variation of the thermoelectric power (S) of material $La_{0.5}Pb_{0.5}MnO_3$ with two different grain sizes, S1 and S3, ($B = 0$ and 1.5 T) at low temperature. [F] Plot of S as a function of temperature, the solid lines represent the best fitting curves with the equation $S = S0 + S1.5\ T\ 1.5 + S4\ T\ 4$. [G] Variation of thermopower S as a function of inverse temperature $1/T$, solid lines are the best fits to Mott's SPH model eqn (28). Reprinted with permission from the AIP Publishing.[145] [H] (i) The calculated normalized resistivity at a specific temperature is plotted as a function of magnetic field strength and orientation relative to the crystal c-axis ($\boldsymbol{\theta}$) (ii) the calculated dependence of normalized resistivity rotating in the yz plane is shown by solid lines, compared with the experimental results obtained from the slab sample (iii and iv) the calculated angle dependence of normalized resistivity rotating in three perpendicular planes (from y to x, z to y, and z to x direction) is depicted, compared with the experimental results (represented by symbols) obtained from the slab and square-rod samples, respectively.[146] Open source PNAS. [I] The T_s depends on the spin (+ and −) for ferromagnetic junctions in the free-electron model. Reprinted with permission from the Elsevier.[36]

Open Access Article. Published on 11 June 2024. Downloaded on 2/18/2026 10:19:39 AM. This article is licensed under a Creative Commons Attribution-NonCommercial 3.0 Unported Licence.

time of conduction electrons. In the research of Kobayashi *et al.*,[144] showed the curves of $\rho(T)$ at $\mu_0 H = 0$ T and $M(T)$ at $\mu_0 H = 0.1$ T exhibit large hysteresis, indicating a first-order transition between AF and F states. At high magnetic field applications, the transition is no longer observed. The results shows that both the normal and extraordinary components at 9 T magnetic field application. Asymmetric scattering affecting the Hall effect can be classified into two mechanisms: the skew scattering proportional to ρ and the side-jump scattering proportional to ρ^2. The extraordinary Hall coefficient R_s for the ferromagnetic state can be described as follows:

$$R_s = a\rho + b\rho^2 \tag{24}$$

$$R_s/\rho = a + b\rho \tag{25}$$

Kobayashi *et al.* explained in their research the relationship between thermoelectric power (S) and temperature under the influence of magnetic fields of 0 and 9 T. At 0 T magnetic field, the curve forms hysteresis indicating a first-order transition. In the ferromagnetic state, S is negative at high temperatures. However, applying a 9 T magnetic field, the ferromagnetic state is observed across the entire temperature range, with S being negative and temperature-dependent. For higher temperatures, the value of S is nearly the same at 0 T and 9 T magnetic fields. According to the Mott equation, the thermoelectric power (S) is formulated as follows:

$$S = \frac{\pi^2 {k_B}^2}{3|e|} T \left[\frac{\partial \ln N(E)}{\partial E} + \frac{\partial \ln \tau(E)}{\partial E}\right]_{E=E_F} \tag{26}$$

$N(E)$ is the density of states, and $\tau(E)$ is the relaxation time of conduction electrons. From the equation, it is evident that S is not dependent on the magnetic field, as the scattering centers do not differ in the transition region. Therefore, the change in the value of S with temperature reflects the change in the energy derivative of the density of states at the Fermi level because of the Fermi surface reconstruction associated with the transition between the AF and F states.[144]

There is a relationship between thermoelectric power (S) and temperature for manganite samples with the influence of grain size. In the study by Banerjee *et al.*,[145] by preparing $La_{0.5}Pb_{0.5}MnO_3$ samples with variations of S1 (heated at 900 °C for 48 h), S2 (the grounded powder was palletized and annealed again at 900 °C for 24 h), and S3 (the well-ground powder is then palletized and annealed at 940 °C for 25 h), grain sizes (S3 > S2 > S1). The curves of S *versus* temperature ($B = 0.0$T and 1.5T) in Fig. 7E for samples S1 and S3 show differences in the S value because of grain size influence. In sample S3, which has lower resistivity, the S value at low temperatures is relatively smaller ($S < 2$ mV) than sample S1. Additionally, samples S1 and S3 also show an increase in S at low temperatures because of the applied magnetic field. Thermoelectric power (S) data dependent on magnetic field in the ferromagnetic region also indicate a contribution from magnons.

Similar to the resistivity data at low temperatures ($T < T_\rho$), the values of S ($B = 0.0$ T and 1.5 T) for the ferromagnetic phase are adjusted according to the following equation:

$$S = S_0 + S_{1.5}T^{1.5} + S_4T^4 \tag{27}$$

where S_0 is S when $T = 0$ K, $T^{1.5}$ behavior suggests that electron–magnon scattering, S_4T^4 is considered to originate from spin wave fluctuations in the FM phase. Fig. 7F shows the best-fit curve (solid line obtained from fitting with eqn (27)). From the curve, it is observed that S ($B = 0.0$ T and 1.5T) decreases with increasing grain size. This is because of the of magnetic domain and grain boundary (GB) scattering mechanisms, which have similar effects on resistivity. Typically, an increase in grain size also leads to an increase in the spin wave fluctuation parameter. This is because larger grain sizes contain magnetic spins with relatively larger fluctuations. However, in reality, thermoelectric power (S) is relatively less sensitive to grain size, as heat flow from one grain to another is naturally additive.

To understand polaronic transport in the paramagnetic phase ($T > T_\rho$), it's necessary to note that the previous S data did not fit well at high temperatures. Therefore, the Mott equation at high temperatures becomes.

Bagian Atas Formulir

$$S = \frac{k_B}{e}\left[\frac{E_s}{k_B T} + \alpha'\right] \tag{28}$$

where E_s is the activation energy from the S, α' is a constant, if $\alpha' < 1$ it indicates jumps influenced by small polarons, and if $\alpha' > 2$ it indicates jumps influenced by large polarons. The Fig. 7G shows the best–fit curve to eqn (28). From the data, the slopes E_s (activation energy) is obtained for samples S1 and S3. The values of E_s are nearly first order of magnitude smaller than those obtained from the resistivity data.[145]

In the AMR effect, we can quantitatively explain it using a phenomenological model influenced by crystal anisotropy. Assuming that the resistivity under the influence of a magnetic field parallel and perpendicular to the c-axis in the crystal is $\rho_\parallel$ and $\rho\perp$, their relationship can be described as follows:

$$\left(\frac{\rho(\Theta)}{\rho_\parallel}\right)^2 \cos^2\Theta + \left(\frac{\rho(\Theta)}{\rho_\perp}\right)^2 \sin^2\Theta = 1 \tag{29}$$

Like in Fig. 7H(i), it shows the short-to-long axial ratio representing the uniaxial resistivity ratio as $\alpha = \rho_\parallel/\rho_\perp$, the resistivity is normalized as in the following equation:

$$\frac{\rho(\Theta)}{\rho_\parallel} = \alpha\left(\alpha^2 \cos^2\Theta + \sin^2\Theta\right)^{-1/2} \tag{30}$$

AMR is fully determined by the ratio α, if the anisotropy is too weak $\alpha = 1$ is assumed. Therefore, the resistivity can be formulated as follows:

$$\frac{\rho(\Theta)}{\rho_\parallel} = \alpha\cos^2\Theta + \alpha\sin^2\Theta \tag{31}$$

The equation describes a symmetric sinusoidal function of the angle Θ.

© 2024 The Author(s). Published by the Royal Society of Chemistry

Open Access Article. Published on 11 June 2024. Downloaded on 2/18/2026 10:19:39 AM. This article is licensed under a Creative Commons Attribution-NonCommercial 3.0 Unported Licence.

In Fig. 7H(ii) and (iii), there is an asymmetry from peak to valley with a broader valley width. Fig. 7H(ii) exhibits a very good agreement between theoretical and experimental results, forming a clearly asymmetric line shape, which provides justification for eqn (31). This emphasizes that AMR also displays asymmetry in the form of $\rho(\Theta)/\rho_0$. The phenomenological model shows consistency across all experimental AMR data for all magnetic field rotations in various sample planes. Fig. 7H(iii) demonstrates excellent agreement between theoretical and experimental results from the slab sample (with dimensions 3.8 $\times$ 0.85 $\times$ 0.15 mm^3). Each component satisfies eqn (31) and exhibits the same values across the samples. Fig. 7H(iv) depict the agreement of the adjusted parameters with the data $\rho(\Theta)/\rho_0$ from square-rod sample (with dimensions 7.0 $\times$ 0.85 $\times$ 0.85 mm^3). The conformity between experimental data and theoretical results indicates a very good fit, despite disregarding other contributions, such as Lorentzian MR.[146]

Next, in the TMR effect, we need to consider a one-dimensional free electron model to investigate the process of electron tunneling through a barrier. Next, we need to calculate the transmission probability for electrons from the left electrode with the energy required to penetrate the barrier towards the right electrode. The required energy (E) is measured from the bottom of the energy band, and its magnitude depends on spin when the electrode is ferromagnetic, expressed as E_s, where $s = +$ (majority spin) and $s = -$ (minority spin).

Then, the barrier potential is denoted by ϕ determined from the Fermi energy and d (barrier thickness). Further, the rate of decrease in the wave function at the barrier can be calculated using the following equation:

$$k = \sqrt{2m\Phi/h} \tag{32}$$

where m is the effective mass of tunneling electrons in a free-electron model. Meanwhereas, the transmission coefficient is calculated using the following equation:

$$T_s = \frac{16E_s\,\Phi}{(E_s + \Phi)^2} e^{-2\kappa d},\ \text{for}\ \kappa d \gg 1 \tag{33}$$

The values of T_s are plotted as a function of ϕ/E_+ to obtain the value of E_+/E_-. Fig. 7I shows that the sign of the spin polarization of the transmission coefficient (T_s) depends on ϕ/E_+.

The difference between the transmission coefficients in parallel (P) and antiparallel (AP) alignments of magnetization also needs to be evaluated, which can be calculated using a generalized calculation such as the conductance Γ_P and Γ_{AP} P for P and AP alignments of the magnetization, as in the following equation:

$$\Gamma_{P(AP)} \propto 1 + (-)P^2 \tag{34}$$

$$P = \left|\frac{k_{F+} - k_{F-}\kappa^2 - k_{F+}k_{F-}}{k_{F+} - k_{F-}\kappa^2 + k_{F+}k_{F-}}\right| \tag{35}$$

With k_{Fs} is the Fermi wave number for the s-spin of the electrodes. Meanwhereas, the MR ratio is determined as MR = (Γ_P $-$ Γ_{AP})/Γ_P.

The value of P needs to be evaluated by calculating k_{Fs}, where P is very small (only a few percent) than experimental measurements involving the factor $|k^2 - k_{F+}k_{F-}|$. To obtain a quantitative comparison between experimental and theoretical values of P, numerical calculations of P should be more realistic, incorporating the effects of disorder at, for example, junction interfaces.[36]

6. Conclusions, challenges and perspectives

The magnetoresistive (MR) properties are highly unique characteristics of magnetic materials and have various applications in different technological fields. MR is observed in several material groups, including perovskites, alloys, spinels, and Kagome magnets. Comparing the properties of each material group, perovskite materials exhibit superior MR values, supported by various magnetic and electrical parameters. Perovskite materials show ideal magnetization curves with high saturation magnetization, low coercivity, and a critical temperature (T_c) close to room temperature. Electrically, perovskite materials can undergo significant changes in resistivity when an external magnetic field is applied. Therefore, perovskite materials are intriguing for development because of their excellent MR properties and the ability to operate at room temperature without the need for cooling.

However, there are still challenges for the widespread potential applications of perovskite materials. Perovskites will exhibit good magnetic properties, electrical properties, and magnetoresistance whereas having T_c near room temperature if substituted with the right cations, both at A and B sites, considering the radii of the substituting elements that will influence the electron transport mechanism in the perovskite material. Therefore, perovskite materials have great potential for further development to enhance their properties and create materials with superior characteristics.

Conflicts of interest

The authors declare no conflict of interest.

Acknowledgements

The authors gratefully acknowledge the PMDSU Scholarship for Okvarahireka Vitayaya and the financial support under grant "Penelitian Dasar Unggulan Perguruan Tinggi 2024" NKB-677/UN2.RST/HKP.05.00/2024.

References

1 X. Y. Qu, X. F. Gou and T. G. Wang, *Comput. Mater. Sci.*, 2021, **193**, 110406.
2 R. Weiss, R. Mattheis and G. Reiss, *Meas. Sci. Technol.*, 2013, **24**, 1–17.
3 S. Yuasa, *J. Phys. Soc. Jpn.*, 2008, **77**, 1–13.
4 K. Takanashi, *Spintron. Next Gener. Innov. Devices*, 2016, 1–20.

Open Access Article. Published on 11 June 2024. Downloaded on 2/18/2026 10:19:39 AM. This article is licensed under a Creative Commons Attribution-NonCommercial 3.0 Unported Licence.

5 Y. Tian and S. Yan, *Sci. China: Phys., Mech. Astron.*, 2013, **56**, 2–14.
6 A. P. Ramirez, *J. Phys.: Condens.Matter*, 1997, **9**, 8171–8199.
7 S. B. Li, C. B. Wang, H. X. Liu, L. Li, Q. Shen, M. Z. Hu and L. M. Zhang, *Mater. Res. Bull.*, 2018, **99**, 73–78.
8 H. Zhang, W. Chen, L. Xie, H. H. Zhao and Q. Li, *Curr. Appl. Phys.*, 2022, **35**, 58–66.
9 V. P. Jovanović, H. Raffy, Z. Z. Li, G. Reményi and P. Monceau, *Phys. Rev. B*, 2021, **103**, 1–9.
10 J. Hemberger, T. Rudolf, H. A. Krug Von Nidda, F. Mayr, A. Pimenov, V. Tsurkan and A. Loidl, *Phys. Rev. Lett.*, 2006, **97**, 2–5.
11 O. Mounkachi, L. Fkhar, R. Lamouri, E. Salmani, A. El hat, M. Hamedoun, H. Ez-Zahraouy, E. K. Hlil, M. Ait Ali and A. Benyoussef, *Ceram. Int.*, 2021, **47**, 31886–31893.
12 S. Routh, I. Kar, A. Low, S. Ghosh and T. Bhowmik, *Phys. Lett. A*, 2023, **468**, 129101.
13 L. Ye, M. Kang, J. Liu, F. Von Cube, C. R. Wicker, T. Suzuki, C. Jozwiak, A. Bostwick, E. Rotenberg, D. C. Bell, L. Fu, R. Comin and J. G. Checkelsky, *Nature*, 2018, **555**, 638–642.
14 M. Kang, L. Ye, S. Fang, J. You, A. Levitan, M. Han and J. I. Facio, *Nat. Mater.*, 2020, **19**, 163–169.
15 D. Chen, C. Le, C. Fu, H. Lin, W. Schnelle, Y. Sun and C. Felser, *Phys. Rev. B*, 2021, **103**, 144410.
16 B. Wang, E. Yi, L. Li, J. Qin, B. Hu, B. Shen and M. Wang, *Phys. Rev. B*, 2022, **106**, 1–7.
17 X. Zhang, H. Zhang, M. Qian and L. Geng, *Sci. Rep.*, 2018, **8**, 1–11.
18 Z. Guo, H. T. Hahn, H. Lin, A. B. Karki and D. P. Young, *J. Appl. Phys.*, 2008, **104**, 1–5.
19 W. J. Gallagher and S. S. P. Parkin, *IBM J. Res. Dev.*, 2006, **50**, 5–23.
20 A. Brataas and P. J. Kelly, *Phys. Rep.*, 2006, **427**, 157–255.
21 X. Yu, S. Jin, X. Guan, Y. Yan, K. Wu, L. Zhao and X. Liu, *J. Alloys Compd.*, 2022, **890**, 161788.
22 L. N. Lau, K. P. Lim, A. N. Ishak, N. B. Ibrahim and M. Miryala, *Coating*, 2021, **11**, 1–15.
23 S. Sarkar, M. De Raychaudhury, I. Dasgupta and T. Saha-Dasgupta, *Phys. Rev. B: Condens. Matter Mater. Phys.*, 2009, **80**, 2–5.
24 F. Canepa, M. Napoletano, C. Lefevre and G. Venturini, *Phys. B*, 2003, **334**, 68–74.
25 C. Liu, H. Zhang, Z. Li, Y. Yan, Y. Zhang, Z. Hou and X. Fu, *Surf. Interfaces*, 2023, **39**, 102866.
26 B. Shi, Z. Zhang, Y. Liu, J. Su, X. Liu, X. Li, J. Wang, M. Zhu, Z. Yang, J. Xu and Y. F. Han, *J. Catal.*, 2020, **381**, 150–162.
27 K. K. Kefeni, T. A. M. Msagati, T. T. Nkambule and B. B. Mamba, *Mater. Sci. Eng. C*, 2020, **107**, 110314.
28 B. Rajyaguru, K. Gadani, M. J. Keshvani, D. Dhruv, A. D. Joshi, K. Asokan, R. J. Choudhary, D. M. Phase, N. A. Shah and P. S. Solanki, *Mater. Res. Bull.*, 2023, **170**, 112548.
29 S. Fan, C. Zhou, H. Xu, J. Xu, H. M. Wen, J. Q. Xiao and J. Hu, *J. Alloys Compd.*, 2022, **910**, 164729.
30 Z. Wang, L. Chen, S. Li, J. Ying, F. Tang, G. Gao, D. Cortie, X. Wang and R. Zheng, *npj Quantum Mater.*, 2021, **53**, 1–8.
31 V. Nabaei, R. Chandrawati and H. Heidari, *Biosens. Bioelectron.*, 2017, **86**, 69–86.
32 M. N. Baibich, J. M. Broto, A. Fert, F. N. Van Dau, F. Petroff, P. Eitenne, G. Creuzet, A. Friederich and J. Chazelas, *Phys. Rev. Lett.*, 1988, **61**, 2472–2475.
33 C. Chappert, A. Fert and F. N. Van Dau, *Nat. Mater.*, 2007, **3**, 1–36.
34 P. M. Levy, S. Zhang and A. Fert, *Phys. Rev. Lett.*, 1990, **65**, 1643–1646.
35 K.-M. H. Lenssen, D. J. Adelerhof, H. J. Gassen, A. E. T. Kuiper and J. B. A. D. van Zon, *Sens. Actuators*, 2000, **85**, 1–8.
36 J. ichiro Inoue, GMR, TMR and BMR, *Nanomagnetism and Spintronics*, 2009.
37 C. L. C. John, Q. Xiao and J. Samuel Jiang, *Phys. Rev. Lett.*, 2008, **70**, 2008–2011.
38 P. K. Siwach, R. Prasad, A. Gaur, H. K. Singh, G. D. Varma and O. N. Srivastava, *J. Alloys Compd.*, 2007, **443**, 26–31.
39 P. Kameli, H. Salamati and A. Aezami, *J. Alloys Compd.*, 2008, **450**, 7–11.
40 D. H. Manh, P. T. Phong, T. D. Thanh, L. V. Hong and N. X. Phuc, *J. Alloys Compd.*, 2010, **499**, 131–134.
41 L. K. Pah, W. Y. Jing, N. Jamaluddin, A. N. Ishak, H. X. Tong, L. L. Nguong, M. M. A. Kechik, C. S. Kien and A. H. Shaari, *Mater. Today: Proc.*, 2023, 3–6.
42 I. K. Yu Zhang1, Y. Ni1, H. Zhao1, S. Hakani2, F. Ye3, L. DeLong4 and G. Ca, *Nature*, 2022, **611**, 467–472.
43 D. Das, A. Saha, S. E. Russek, R. Raj and D. Bahadur, *J. Appl. Phys.*, 2003, **93**, 8301–8302.
44 C. Jooss, L. Wu, T. Beetz, R. F. Klie, M. Beleggia, M. A. Schofield, S. Schramm, J. Hoffmann and Y. Zhu, *Proc. Natl. Acad. Sci. U. S. A.*, 2007, **104**, 13597–13602.
45 G. Subías, J. Blasco, V. Cuartero, S. Lafuerza, L. Simonelli, G. Gorni, M. Castro and J. García, *Phys. Rev. B*, 2023, **107**, 1–13.
46 C. H. Booth, F. Bridges, G. H. Kwei, J. M. Lawrence, A. L. Cornelius and J. J. Neumeier, *Phys. Rev. Lett.*, 1998, **80**, 853–856.
47 A. Dhahri, *J. Mol. Struct.*, 2023, **3**, 136592.
48 J. M. D. Coey, A. E. Berkowitz, L. Balcells, F. F. Putris and F. T. Parker, *Appl. Phys. Lett.*, 1998, **72**, 734–736.
49 J. Barnaś and W. Rudziński, *Phys. Rev. B: Condens. Matter Mater. Phys.*, 2001, **64**, 1–10.
50 T. Ichinose, J. Ikeda, Y. Onodera, T. Tsuchiya, K. Z. Suzuki and S. Mizukami, *J. Alloys Compd.*, 2023, **960**, 170750.
51 H. Gu, X. Zhang, H. Wei, Y. Huang, S. Wei and Z. Guo, *Chem. Soc. Rev.*, 2013, **42**, 5907–5943.
52 H. S. Alagoz, J. Desomberg, M. Taheri, F. S. Razavi, K. H. Chow and J. Jung, *Appl. Phys. Lett.*, 2015, **106**, 082407.
53 J. Velev, R. F. Sabirianov, S. S. Jaswal and E. Y. Tsymbal, *Phys. Rev. Lett.*, 2005, **94**, 1–4.
54 R. L. Greene, H. L. Ju, J. Gopalakrishnan, J. L. Peng, L. Qi, G. C. Xiong and T. Venkatesan, *Phys. Rev. B: Condens. Matter Mater. Phys.*, 1995, **51**, 6143–6146.
55 A. Gupta and J. Z. Sun, *J. Magn. Magn. Mater.*, 1999, **200**, 24–43.

© 2024 The Author(s). Published by the Royal Society of Chemistry

Open Access Article. Published on 11 June 2024. Downloaded on 2/18/2026 10:19:39 AM. This article is licensed under a Creative Commons Attribution-NonCommercial 3.0 Unported Licence.

56 I. P. Muthuselvam and R. N. Bhowmik, *J. Alloys Compd.*, 2012, **511**, 22–30.
57 G. Giovannetti, S. Kumar, J. Van Den Brink and S. Picozzi, *Phys. Rev. Lett.*, 2009, **103**, 1–4.
58 A. Goktas, I. H. Mutlu and A. Kawashi, *Thin Solid Films*, 2012, **520**, 6138–6144.
59 S. Joseph and K. V. Saban, *Ceram. Int.*, 2019, **45**, 6425–6439.
60 E. S. Bozin, W. G. Yin, R. J. Koch, M. Abeykoon, Y. S. Hor, H. Zheng, H. C. Lei, C. Petrovic, J. F. Mitchell and S. J. L. Billinge, *Nat. Commun.*, 2019, **10**, 1–7.
61 R. Mahesh, R. Mahendiran, A. K. Raychaudhuri and C. N. R. Rao, *J. Solid State Chem.*, 1995, **114**, 297–299.
62 K. Kuepper, M. C. Falub, K. C. Prince, V. R. Galakhov, I. O. Troyanchuk, S. G. Chiuzbaian, M. Matteucci, D. Wett, R. Szargan, N. A. Ovechkina, Y. M. Mukovskii and M. Neumann, *J. Phys. Chem. B*, 2005, **109**, 9354–9361.
63 J. Ahmad, H. Abbas, S. H. Bukhari, M. T. Jamil, U. Nissar, J. A. Khan and S. A. Ali, *J. Ovonic Res.*, 2018, **14**, 429–439.
64 Y. Tang, F. Chiabrera, A. Morata, A. Cavallaro, M. O. Liedke, H. Avireddy, M. Maller, M. Butterling, A. Wagner and M. Stchakovsky, *ACS Appl. Mater. Interfaces*, 2022, **14**, 18486–18497.
65 S. Koner, S. Satapathy, P. Deshmukh, R. K. Sharma, P. K. Sahoo and S. K. Majumder, *J. Alloys Compd.*, 2023, **968**, 172249.
66 O. Y. Gorbenko, O. V. Melnikov, A. R. Kaul, A. M. Balagurov, S. N. Bushmeleva, L. I. Koroleva and R. V. Demin, *Mater. Sci. Eng., B*, 2005, **116**, 64–70.
67 T. Manabe, T. Fujimoto, I. Yamaguchi, W. Kondo, I. Kojima, S. Mizuta and T. Kumagai, *Thin Solid Films*, 1998, **323**, 99–104.
68 D. R. Munazat, B. Kurniawan, D. S. Razaq, K. Watanabe and H. Tanaka, *Phys. B*, 2020, **592**, 412227.
69 S. O. Manjunatha, A. Rao, T. Y. Lin, C. M. Chang and Y. K. Kuo, *J. Alloys Compd.*, 2015, **619**, 303–310.
70 J. B. Goodenough, *J. Less-Common Met.*, 1986, **116**, 83–93.
71 Y. Kalyana Lakshmi, G. Venkataiah, M. Vithal and P. Venugopal Reddy, *Phys. B*, 2008, **403**, 3059–3066.
72 G. Venkataiah and P. V. Reddy, *Solid State Commun.*, 2005, **136**, 114–119.
73 G. Venkataiah, V. Prasad and P. Venugopal Reddy, *J. Alloys Compd.*, 2007, **429**, 1–9.
74 X. Xiao, S. L. Yuan, Y. Q. Wang, G. M. Ren, J. H. Miao, G. Q. Yu, Z. M. Tian, L. Liu, L. Chen and S. Y. Yin, *Solid State Commun.*, 2007, **141**, 348–353.
75 T. D. Thanh, L. H. Nguyen, D. H. Manh, N. V. Chien, P. T. Phong, N. V. Khiem, L. V. Hong and N. X. Phuc, *Phys. B*, 2012, **407**, 145–152.
76 R. Rozilah, N. Ibrahim and A. K. Yahya, *Solid State Sci.*, 2019, **87**, 64–80.
77 S. W. Ng, K. P. Lim, S. A. Halim and H. Jumiah, *Results Phys.*, 2018, **9**, 1192–1200.
78 A. E. Danks, S. R. Hall and Z. Schnepp, *Mater. Horiz.*, 2016, **3**, 91–112.
79 D. R. Munazat, B. Kurniawan, D. S. Razaq, K. Watanabe and H. Tanaka, *Phys. B*, 2020, **592**, 412227.
80 Z. Wu, W. Zhou, W. Jin and N. Xu, *AIChE J.*, 2006, **52**, 769–776.
81 A. Das, K. Kumar Bestha, P. Bongurala and V. Gorige, *Nanotechnology*, 2020, **31**, 335716.
82 J. Massoudi, M. Smari, K. Nouri, E. Dhahri, K. Khirouni, S. Bertaina, L. Bessais and E. K. Hlil, *RSC Adv.*, 2020, **10**, 34556–34580.
83 A. Swain, P. S. Anil Kumar and V. Gorige, *J. Magn. Magn. Mater.*, 2019, **485**, 358–368.
84 H. Chen, C. Jin, X. Song, P. Wang, L. Chen and H. Bai, *Appl. Surf. Sci.*, 2021, **569**, 151032.
85 H. Cheng, H. Chen, C. Jin and H. Bai, *J. Magn. Magn. Mater.*, 2023, **565**, 170300.
86 U. K. Sinha, A. Sahoo and P. Padhan, *J. Alloys Compd.*, 2023, **952**, 170037.
87 L. Yin, C. Wang and Q. Shen, *Ceram. Int.*, 2023, **49**, 1–9.
88 R. C. Bhatt, S. K. Singh, P. C. Srivastava, S. K. Agarwal and V. P. S. Awana, *J. Alloys Compd.*, 2013, **580**, 377–381.
89 N. Panwar, I. Coondoo, R. S. Singh and S. K. Agarwal, *J. Alloys Compd.*, 2010, **507**, 439–442.
90 N. Ibrahim and A. K. Yahya, *Ceram. Int.*, 2013, **39**, S181–S184.
91 J. Lloyd-Hughes, C. D. W. Mosley, S. P. P. Jones, M. R. Lees, A. Chen, Q. X. Jia, E. M. Choi and J. L. MacManus-Driscoll, *Nano Lett.*, 2017, **17**, 2506–2511.
92 M. Kumar Verma, N. Dutt Sharma, S. Sharma, N. Choudhary and D. Singh, *Mater. Res. Bull.*, 2020, **125**, 110813.
93 A. De Andrés, M. García-Hernández and J. L. Martínez, *Phys. Rev. B: Condens. Matter Mater. Phys.*, 1999, **60**, 7328–7334.
94 P. T. Phong, D. H. Manh, N. V. Dang, L. V. Hong and I. J. Lee, *Phys. B*, 2012, **407**, 3774–3780.
95 B. Rajyaguru, K. Gadani, M. J. Keshvani, D. Dhruv, A. D. Joshi, K. Asokan, R. J. Choudhary, D. M. Phase, N. A. Shah and P. S. Solanki, *Mater. Res. Bull.*, 2024, **170**, 112548.
96 M. Wali, R. Skini, M. Khlifi, M. Bekri, E. Dhahri and E. K. Hlil, *Ceram. Int.*, 2016, **42**, 5699–5706.
97 M. Khlifi, E. Dhahri and E. K. Hlil, *J. Alloys Compd.*, 2014, **587**, 771–777.
98 S. Samanta, S. Ghosh, S. Chatterjee and K. Mandal, *J. Alloys Compd.*, 2022, **910**, 164929.
99 A. Costas, C. Florica, E. Matei, M. E. Toimil-Molares, I. Stavarache, A. Kuncser, V. Kuncser and I. Enculescu, *Beilstein J. Nanotechnol.*, 2018, **9**, 2345–2355.
100 H. Zhang, M. Qian, X. Zhang, L. Wei, F. Cao, D. Xing, X. Cui, J. Sun and L. Geng, *J. Alloys Compd.*, 2016, **689**, 481–488.
101 A. S. R. Modak, *Appl. Phys.*, 2019, 125.
102 H. Zhang, X. Zhang, Y. Xiao, M. Yang, Z. Xu, Z. Yao, M. Qian, L. Zhang, L. Yin and D. Jia, *Intermetallics*, 2022, **149**, 107651.
103 S. C. Ma, D. H. Wang, Z. C. Zhong, J. M. Luo, J. L. Xu and Y. W. Du, *Appl. Phys. Lett.*, 2013, **102**, 3–7.
104 S. C. Ma, D. Hou, Y. Y. Gong, L. Y. Wang, Y. L. Huang, Z. C. Zhong, D. H. Wang and Y. W. Du, *Appl. Phys. Lett.*, 2014, **104**, 1–6.

© 2024 The Author(s). Published by the Royal Society of Chemistry

Open Access Article. Published on 11 June 2024. Downloaded on 2/18/2026 10:19:39 AM. This article is licensed under a Creative Commons Attribution-NonCommercial 3.0 Unported Licence.

105 S. Pandey, A. Quetz, A. Aryal, I. Dubenko, D. Mazumdar, S. Stadler and N. Ali, *Magnetochemistry*, 2017, **3**, 1–7.
106 L. Ma, W. H. Wang, C. M. Zhen, D. L. Hou, X. D. Tang, E. K. Liu and G. H. Wu, *Phys. Rev. B: Condens. Matter Mater. Phys.*, 2011, **84**, 1–9.
107 X. Y. Z. X. Cr, Y. Co, Z. Al, S. K. Mohanta, Y. Tao, X. Yan, G. Qin and V. Chandragiri, *J. Magn. Magn. Mater.*, 2017, **430**, 65–69.
108 X. P. Wei, Y. L. Zhang, X. W. Sun, T. Song, P. Guo, Y. Gao, J. L. Zhang, X. F. Zhu and J. B. Deng, *J. Alloys Compd.*, 2017, **694**, 1254–1259.
109 H. Arshad, M. Zafar, S. Ahmad, M. Rizwan, M. I. Khan, S. S. A. Gillani, C. B. Cao and M. Shakil, *Mod. Phys. Lett. B*, 2019, **33**, 1950389.
110 S. A. Khandy, I. Islam, D. C. Gupta and A. Laref, *J. Solid State Chem.*, 2019, **270**, 173–179.
111 H. Xie, H. Wang, C. Fu, Y. Liu, G. J. Snyder, X. Zhao and T. Zhu, *Sci. Rep.*, 2014, **4**, 1–6.
112 M. Shakil, S. Mushtaq, I. Zeba, S. S. A. Gillani, M. I. Khan, H. Arshad and M. Rafique, *Phys. B*, 2021, **602**, 412558.
113 C. Felser, L. Wollmann, S. Chadov, G. H. Fecher and S. S. P. Parkin, *APL Mater.*, 2015, **3**, 041518.
114 L. Chen, F. X. hu, J. Wang, J. Shen, J. Zhang, J. R. Sun, B. G. Shen, J. H. Yin and L. Q. Pan, *J. Appl. Phys.*, 2010, **107**, 2472.
115 R. Sahoo, A. K. Nayak, K. G. Suresh and A. K. Nigam, *Appl. Phys.*, 2011.
116 Z. Ni, X. Guo, X. Liu, Y. Jiao, F. Meng and H. Luo, *J. Alloys Compd.*, 2019, **775**, 427–434.
117 Y. Wu, H. Xuan, S. Agarwal, Y. Xu, T. Zhang, L. Feng, H. Li, P. Han, C. Zhang, D. Wang, F. Chen and Y. Du, *Phys. Status Solidi A*, 2018, **215**, 1–7.
118 S. C. Ma, D. H. Wang, Z. C. Zhong, J. M. Luo, J. L. Xu and Y. W. Du, *Appl. Phys. Lett.*, 2013, **102**, 1–6.
119 R. Kainuma, W. Ito, R. Y. Umetsu, K. Oikawa and K. Ishida, *Appl. Phys. Lett.*, 2008, **93**, 2008–2010.
120 S. Chatterjee, S. Giri, S. Majumdar and S. K. De, *Phys. Rev. B: Condens. Matter Mater. Phys.*, 2008, **77**, 1–5.
121 K. Dey, A. Indra, A. Karmakar and S. Giri, *J. Magn. Magn. Mater.*, 2020, **498**, 166090.
122 S. Roy, H. R. Nikhita, G. V. Varshini, A. Kumar Patra, R. B. Gangineni and S. Angappane, *J. Magn. Magn. Mater.*, 2022, **557**, 169468.
123 H. Sharifi Dehsari, A. Halda Ribeiro, B. Ersöz, W. Tremel, G. Jakob and K. Asadi, *CrystEngComm*, 2017, **19**, 6694–6702.
124 G. U. Kulkarni, K. R. Kannan and T. Arunarkavalli, *Phys. Rev.*, 1994, **49**, 4–7.
125 I. M. Obaidat, B. Issa and Y. Haik, *Nanomaterials*, 2014, **5**, 63–89.
126 O. Mounkachi, M. Hamedoun and A. Benyoussef, *J. Supercond. Novel Magn.*, 2017, **30**, 3035–3038.
127 S. Ju, K. W. Yu and Z. Y. Li, *Phys. Rev. B: Condens. Matter Mater. Phys.*, 2005, **71**, 1–8.
128 A. Gaur and G. D. Varma, *J. Phys.: Condens.Matter*, 2006, **18**, 8837–8846.
129 I. A. Abdel-Latif, A. M. Ahmed, H. F. Mohamed, S. A. Saleh, J. A. Paixão, K. A. Ziq, M. K. Hamad, E. G. Al-Nahari, M. Ghozza and S. Allam, *J. Magn. Magn. Mater.*, 2018, **457**, 126–134.
130 A. K. M. Akther Hossain, H. Tabata and T. Kawai, *J. Magn. Magn. Mater.*, 2008, **320**, 1157–1162.
131 A. K. M. A. Hossain, M. Seki, T. Kawai and H. Tabata, *J. Appl. Phys.*, 2004, **96**, 1273–1275.
132 J. Hu, H. Qin, Y. Wang, Z. Wang and S. Zhang, *Solid State Commun.*, 2000, **115**, 233–235.
133 L. Fkhar, K. El Maalam, M. Hamedoun, A. El Kenz, A. Benyoussef, P. Lachkar, E. K. Hlil, A. Mahmoud, F. Boschini, M. Ait Ali and O. Mounkachi, *Mater. Res. Express*, 2020, **7**, 9.
134 W. Ma, X. Xu, J. Yin, H. Yang, H. Zhou, Z. Cheng and Y. Huang, *Phys. Rev. Lett.*, 2021, 3–8.
135 D. Das, C. M. Srivastava, D. Bahadur, A. K. Nigam and S. K. Malik, *J. Phys.: Condens.Matter*, 2004, **16**, 4089–4102.
136 L. H. Nguyen, L. X. Hung, N. X. Phuc, P. H. Nam, L. T. T. Ngan, N. V. Dang, L. V. Bau, P. H. Linh and P. T. Phong, *J. Alloys Compd.*, 2020, **849**, 1–10.
137 M. Viret, L. Ranno and J. Coey, *Phys. Rev. B: Condens. Matter Mater. Phys.*, 1997, **55**, 8067–8070.
138 S. Asthana, D. Bahadur, A. K. Nigam and S. K. Malik, *J. Phys.: Condens.Matter*, 2004, **16**, 5297–5307.
139 M. Khlifi, E. Dhahri and E. K. Hlil, *J. Alloys Compd.*, 2014, **587**, 771–777.
140 M. Ziese, *Phys. Rev. B: Condens. Matter Mater. Phys.*, 2003, **68**, 7–10.
141 G. Cao, Y. Li, J. Zhang, S. Cao, C. Cai and X. Shen, *J. Appl. Phys.*, 2010, **107**, 2–7.
142 Y. Xu, J. Zhang, G. Cao, C. Jing and S. Cao, *Phys. Rev. B: Condens. Matter Mater. Phys.*, 2006, **73**, 2–7.
143 A. G. Gamzatov and I. K. Kamilov, *J. Alloys Compd.*, 2012, **513**, 334–338.
144 Y. Kobayashi, K. Muta and K. Asai, *J. Phys.: Condens.Matter*, 2001, **13**, 3335–3346.
145 A. Banerjee, S. Pal, S. Bhattacharya, B. K. Chaudhuri and H. D. Yang, *J. Appl. Phys.*, 2002, **91**, 5125–5134.
146 R. W. Li, H. Wang, X. Wang, X. Z. Yu, Y. Matsui, Z. H. Cheng, B. G. Shen, E. W. Plummere and J. Zhang, *Proc. Natl. Acad. Sci. U. S. A.*, 2009, **106**, 14224–14229.
147 Z. S. Popović and F. R. Vukajlović, *Phys. Rev. Lett.*, 1996, **76**, 960–963.
148 M. Kumar Verma, N. Dutt Sharma, S. Sharma, N. Choudhary and D. Singh, *Mater. Res. Bull.*, 2020, **125**, 110813.
149 R. Dhahri and F. Halouni, *J. Alloys Compd.*, 2004, **381**, 21–25.
150 R. Suryanarayanan, J. Berthon, I. Zelenay, B. Martinez, X. Obradors, S. Uma and E. Gmelin, *J. Appl. Phys.*, 1998, **83**, 5264–5269.
151 X. Yu, S. Jin, H. Li, X. Guan, X. Gu and X. Liu, *Appl. Surf. Sci.*, 2021, **570**, 151221.
152 G. Venkataiah, Y. K. Lakshmi, V. Prasad and P. V. Reddy, *J. Nanosci. Nanotechnol.*, 2007, **7**, 2000–2004.
153 Y. Zhou, X. Zhu and S. Li, *Ceram. Int.*, 2017, **43**, 3679–3687.
154 A. P. Ramirez, S. W. Cheong and P. Schiffer, *J. Appl. Phys.*, 1997, **81**, 5337–5342.

© 2024 The Author(s). Published by the Royal Society of Chemistry

Open Access Article. Published on 11 June 2024. Downloaded on 2/18/2026 10:19:39 AM. This article is licensed under a Creative Commons Attribution-NonCommercial 3.0 Unported Licence.

155 X. Yu, H. Li, K. Chu, X. Pu, X. Gu, S. Jin, X. Guan and X. Liu, *Ceram. Int.*, 2021, **47**, 13469–13479.
156 P. Schiffer, A. P. Ramirez, W. Bao and S. W. Cheong, *Phys. Rev. Lett.*, 1995, **75**, 3336–3339.
157 G. Venkataiah, J. C. A. Huang and P. Venugopal Reddy, *J. Magn. Magn. Mater.*, 2010, **322**, 417–423.
158 P. Dey and T. K. Nath, *Phys. Rev. B: Condens. Matter Mater. Phys.*, 2006, **73**, 1–14.
159 R. Das and R. Mahendiran, *Ceram. Int.*, 2021, **47**, 393–399.
160 S. Jin, X. Gu, X. Yu, X. Guan, Y. Yan, K. Wu, L. Zhao, Y. Zhu, S. Sun, J. Liu, J. Hu, J. Zhao, L. Kong, W. Yang, Q. Chen, P. Kameli and X. Liu, *Appl. Surf. Sci.*, 2022, **589**, 152905.
161 W. Jian, *J. Magn. Magn. Mater.*, 2012, **324**, 2183–2187.
162 S. Das and T. K. Dey, *Solid State Commun.*, 2005, **134**, 837–842.
163 Y. Ng-Lee, F. Sapiña, E. Martinez-Tamayo, J. V. Folgado, R. Ibañez, D. Beltrán, F. Lloret and A. Segura, *J. Mater. Chem.*, 1997, **7**, 1905–1909.
164 K. Y. Pan, S. A. Halim, K. P. Lim, W. M. W. Y. Daud, S. K. Chen and M. Navasery, *J. Mater. Sci.: Mater. Electron.*, 2013, **24**, 1869–1874.
165 G. Popov, J. Goldsmith and M. Greenblatt, *J. Solid State Chem.*, 2003, **175**, 52–58.
166 S. Asthana, A. K. Nigam, S. K. Malik and D. Bahadur, *J. Alloys Compd.*, 2008, **450**, 136–141.
167 D. Varshney and N. Dodiya, *J. Mater. Res.*, 2014, **29**, 1183–1198.
168 L. Dhal, E. Andharia, N. Shukla, T. Geetha Kumary, A. K. Nigam, S. K. Malik, P. N. Santhosh and R. Nirmala, *J. Magn. Magn. Mater.*, 2019, **474**, 215–220.
169 I. D. Mahmud Khan, A. K. Pathak, M. R. Paudel and N. A. Shane Stadler, *J. Magn. Magn. Mater.*, 2008, **320**, L21–L25.
170 X. Zhang, Z. Liu, Q. Cui, Q. Guo, N. Wang, L. Shi, H. Zhang, W. Wang, X. Dong, J. Sun, Z. Dun and J. Cheng, *Phys. Rev. Mater.*, 2022, **6**, 1–9.
171 X. Wei, C. Tian, H. Cui, Y. Li, S. Liu, Y. Feng, J. Cui, Y. Song, Z. Wang and J. H. Chen, *2D Mater.*, 2023, **10**, 1–10.
172 D. Huang, H. Li, B. Ding, X. Xi, J. Gao, Y. C. Lau and W. Wang, *Appl. Phys. Lett.*, 2022, **121**, 232404.
173 K. Jin, G. He, X. Zhang, S. Maruyama, S. Yasui, R. Suchoski, J. Shin, Y. Jiang, H. S. Yu, J. Yuan, L. Shan, F. V Kusmartsev, R. L. Greene and I. Takeuchi, *Nat. Commun.*, 2015, **6**, 7183.
174 C. P. Sun, C. L. Huang, C. C. Lin, J. L. Her, C. J. Ho, J. Y. Lin, H. Berger and H. D. Yang, *Appl. Phys. Lett.*, 2010, **96**, 4–6.
175 H. Aireddy, S. Guchhait and A. K. Das, *J. Magn. Magn. Mater.*, 2022, **556**, 169438.
176 K. Vijay, L. S. S. Chandra, K. Ali, A. Sagdeo, P. Tiwari, M. K. Chattopadhyay, A. Arya and S. Banik, *Appl. Phys. Lett.*, 2023, **122**, 233103.
177 M. A. McGuire, Q. Zhang, H. Miao, W. Luo, M. Yoon, Y. Liu, T. Yilmaz and E. Vescovo, *Chem. Mater.*, 2021, **33**, 9741–9749.
178 Q. Wang, S. Sun, X. Zhang, F. Pang and H. Lei, *Phys. Rev. B*, 2016, **94**, 1–5.
179 C. Q. Xu, T. W. Heitmann, H. Zhang, X. Xu and X. Ke, *Phys. Rev. B*, 2021, **104**, 1–8.
180 H. Fang, M. Lyu, H. Su, J. Yuan, Y. Li, L. Xu, S. Liu, L. Wei, X. Liu, H. Yang, Q. Yao, M. Wang, Y. Guo, W. Shi, Y. Chen, E. Liu and Z. Liu, *Sci. China Mater.*, 2023, **66**, 2032–2038.
181 Y. Wang, G. T. McCandless, X. Wang, K. Thanabalasingam, H. Wu, D. Bouwmeester, H. S. J. Van Der Zant, M. N. Ali and J. Y. Chan, *Chem. Mater.*, 2022, **34**, 7337–7343.

© 2024 The Author(s). Published by the Royal Society of Chemistry